Theses and Dissertations

Fall 2009

# Live cell imaging technology development for cancer research

Elizabeth Anne Kosmacek
*University of Iowa*

Recommended Citation

Kosmacek, Elizabeth Anne. "Live cell imaging technology development for cancer research." PhD (Doctor of Philosophy) thesis, University of Iowa, 2009.
http://ir.uiowa.edu/etd/388.

LIVE CELL IMAGING TECHNOLOGY DEVELOPMENT FOR CANCER

RESEARCH

by

Elizabeth Anne Kosmacek

An Abstract

Of a thesis submitted in partial fulfillment
of the requirements for the Doctor of
Philosophy degree in Biomedical Engineering
in the Graduate College of
The University of Iowa

December 2009

Thesis Supervisor:  Assistant Professor Fiorenza Ianzini

ABSTRACT

Live cell imaging is a unique tool for cellular research with a wide variety of applications. By streaming digital microscopic images an investigator can observe the dynamic morphology of a cell, track cell movement on a surface, and measure quantities or localization patterns of fluorescently labeled proteins or molecules. Digital image sequences contain a vast amount of information in the form of visually detectable morphological changes in the cell. We designed computer programs that allow the manual identification of visible events in live cell digital image sequences [Davis *et al.* 2007]. Once identified, the data are analyzed using algorithms to calculate the yield of individual events *per* cell over the time course of image acquisition. The sequence of event data is also constructed into directed acyclic graphs and through the use of a subgraph isomorphism algorithm we are able to detect specified patterns of events originating from a single cell. Two projects in the field of cancer research are here discussed that describe and validate the application of the event analysis programs. In the first project, mitotic catastrophe (MC) research [Ianzini and Mackey, 1997; Ianzini and Mackey, 1998; reviewed by Ianzini and Mackey, 2007] is enhanced with the addition of live cell imaging to traditional laboratory experiments. The event analysis program is used to describe the yield of normal or abnormal divisions, fusions, and cell death, and to detect patterns of reductive division and depolyploidization in cells undergoing radiation-induced MC. Additionally, the biochemical and molecular data used in conjunction with live cell imaging data are presented to illustrate the usefulness of combining biology and engineering techniques to elucidate pathways involved in cell survival under different detrimental cell conditions. The results show that the timing of depolyploidization in MC cells correlates with increased multipolar divisions, up-regulation of meiosis-specific genes, and the production of mononucleated cell progeny. It was confirmed that mononucleated cells are produced from multipolar divisions and these cells are capable of resuming normal divisions [Ianzini *et al*., 2009]. The implications for the induction of

meiosis as a mechanism of survival after radiation treatment are discussed. In the second project, the effects of long-term fluorescence excitation light exposure are examined through measurements of cell division and cell death. In the field of live cell imaging, probably the most modern and most widely utilized technique is fluorescence detection for intracellular organelles, proteins, and molecules. While the technologies required to label and detect fluorescent molecules in a cell are well developed, they are not idealized for long term measurements as both the probes and excitation light are toxic to the cells [Wang and Nixon, 1978; Bradley and Sharkey, 1977]. From the event analysis data it was determined that fluorescence excitation light is toxic to multiple cell lines observed as the reduction of normal cell division, induction of cell death, and apparent morphological aberrations.

Abstract Approved: _____

Thesis Supervisor

_____

Title and Department

_____

Date

LIVE CELL IMAGING TECHNOLOGY DEVELOPMENT FOR CANCER

RESEARCH

by

Elizabeth Anne Kosmacek

A thesis submitted in partial fulfillment
of the requirements for the Doctor of
Philosophy degree in Biomedical Engineering
in the Graduate College of
The University of Iowa

December 2009

Thesis Supervisor:  Assistant Professor Fiorenza Ianzini

Graduate College
The University of Iowa
Iowa City, Iowa

CERTIFICATE OF APPROVAL

_____

PH.D. THESIS

_____

This is to certify that the Ph.D. thesis of

Elizabeth Anne Kosmacek

has been approved by the Examining Committee
for the thesis requirement for the Doctor of Philosophy
degree in Biomedical Engineering at the December 2009 graduation.

Thesis Committee: _____
                    Fiorenza Ianzini, Thesis Supervisor

                    _____
                    Michael A. Mackey

                    _____
                    Joseph M. Reinhardt

                    _____
                    Tae-Hong Lim

                    _____
                    Thomas L. Casavant

To my family at home and at school.

# ACKNOWLEDGMENTS

ABSTRACT

Live cell imaging is a unique tool for cellular research with a wide variety of applications. By streaming digital microscopic images an investigator can observe the dynamic morphology of a cell, track cell movement on a surface, and measure quantities or localization patterns of fluorescently labeled proteins or molecules. Digital image sequences contain a vast amount of information in the form of visually detectable morphological changes in the cell. We designed computer programs that allow the manual identification of visible events in live cell digital image sequences [Davis *et al.* 2007]. Once identified, the data are analyzed using algorithms to calculate the yield of individual events *per* cell over the time course of image acquisition. The sequence of event data is also constructed into directed acyclic graphs and through the use of a subgraph isomorphism algorithm we are able to detect specified patterns of events originating from a single cell. Two projects in the field of cancer research are here discussed that describe and validate the application of the event analysis programs. In the first project, mitotic catastrophe (MC) research [Ianzini and Mackey, 1997; Ianzini and Mackey, 1998; reviewed by Ianzini and Mackey, 2007] is enhanced with the addition of live cell imaging to traditional laboratory experiments. The event analysis program is used to describe the yield of normal or abnormal divisions, fusions, and cell death, and to detect patterns of reductive division and depolyploidization in cells undergoing radiation-induced MC. Additionally, the biochemical and molecular data used in conjunction with live cell imaging data are presented to illustrate the usefulness of combining biology and engineering techniques to elucidate pathways involved in cell survival under different detrimental cell conditions. The results show that the timing of depolyploidization in MC cells correlates with increased multipolar divisions, up-regulation of meiosis-specific genes, and the production of mononucleated cell progeny. It was confirmed that mononucleated cells are produced from multipolar divisions and these cells are capable of resuming normal divisions [Ianzini *et al.*, 2009]. The implications for the induction of

meiosis as a mechanism of survival after radiation treatment are discussed.  In the second project, the effects of long-term fluorescence excitation light exposure are examined through measurements of cell division and cell death.  In the field of live cell imaging, probably the most modern and most widely utilized technique is fluorescence detection for intracellular organelles, proteins, and molecules.  While the technologies required to label and detect fluorescent molecules in a cell are well developed, they are not idealized for long term measurements as both the probes and excitation light are toxic to the cells [Wang and Nixon, 1978; Bradley and Sharkey, 1977].  From the event analysis data it was determined that fluorescence excitation light is toxic to multiple cell lines observed as the reduction of normal cell division, induction of cell death, and apparent morphological aberrations.

TABLE OF CONTENTS

LIST OF TABLES

Table

LIST OF FIGURES

Figure

CHAPTER 1

BACKGROUND AND RESEARCH PURPOSE

Live Cell Imaging Technology

Live cell imaging is a unique tool for cellular research with a wide variety of applications. By streaming digital microscopic images an investigator can observe the dynamic morphology of a cell, track cell movement on a surface, and measure quantities or localization patterns of fluorescently labeled proteins or molecules [Stephens DJ and Allan V, 2003]. The use of imaging is not a new technology, but long term observation of cells in time lapse microscopy is still an under-developed technique. Commercial live cell imaging systems provide at most a few days of unperturbed cell growth and these systems typically utilize confocal fluorescence technology which is known to induce cell death after only one hour of imaging [Martin *et al*., 2003]. Modern techniques for imaging live cells often use cells growing on glass coverslips or in specialized imaging chambers [Goldman and Spector, 2005; Hinchcliffe, 2005] however, these conditions change the cells' substrate for attachment and represents a deviation from the usual laboratory cell growth conditions. Additionally, the commercially available imaging chambers limit the culture medium present on the cells. Limited media volumes can experience spikes in temperature and drastic pH changes which are both detrimental to the cell culture. To offset the "side-effects" of small medium volumes, oils and/or buffers are sometimes added to the medium [Goldman and Spector, 2005]. Altering cell medium composition introduces another change into the normally used conditions for cell growth in the laboratory setting and limits comparison of the events observed in live cell imaging with those observed in the wet lab. As research scientists desire longer image acquisition periods to observe cellular processes, it is important to maintain a high standard for non-perturbing measurements.

<u>The Large Scale Digital Cell Analysis System (LSDCAS):</u>

<u>Non-Perturbing Live Cell Imaging</u>

LSDCAS is an automated live cell imaging system capable of examining thousands of living cells for up to one month during a single experiment [Ianzini and Mackey 2002; Davis *et al.* 2007]. LSDCAS consists of two live cell imaging systems capable of both phase-contrast and epi-fluorescence imaging (Figure 1.1). System 1 is comprised of an Olympus IX-70 inverted microscope, a Basler A630F CCD camera, and a custom built heat-controlled Plexiglas stage incubator. System 2 includes an Olympus IX-71 inverted phase microscope, a Hamamatsu ORCA-285 cooled CCD camera, and an Okolab stage incubator capable of regulating $CO_2$, humidity, and temperature. In both systems the stage movement, illumination, auto-focusing, and image acquisition are under computer control for fully automated live cell imaging.

LSDCAS is designed for quantitative study of cell culture populations grown under conditions that mimic a traditional incubator used in routine biochemical and molecular *in vitro* experiments. Using a stage incubator we can maintain 95% humidity to prevent medium evaporation, 5% $CO_2$ atmosphere to control pH, and a stable temperature of 37˚C. By using phase-contrast imaging we are able to image adherent cells growing on tissue culture plastic, providing the exact same substrate for cell attachment as is used to maintain the culture in the wet laboratory. We believe that by recreating the environment of a typical air-$CO_2$ incubator we can more reliably combine the results obtained in our live cell imaging experiments with those obtained from traditional experiments in the laboratory. In fact, comparisons of cell doubling time and cell morphology confirm that the cells behave in exactly the same manner during imaging with LSDCAS, as when they are normally maintained in an incubator. With the knowledge that cells are dividing normally during imaging, we observed that visible geometric and optical changes occur as cells divide, and also at death. The potential to

make meaningful measurements from the image data was recognized and described here is the evolution and application of novel tools for live cell image analysis.

We designed computer programs to allow for manual identification of visible events in live cell digital image sequences [Davis *et al.* 2007]. Once identified the data are analyzed with programs to calculate the yield of individual events or to detect patterns of events originating from a single cell [Kosmacek *et al.*, 2009, submitted]. The programs are demonstrated here through their application to two projects in the field of cancer research. In the first project, mitotic catastrophe (MC) research is enhanced with the addition of live cell imaging to traditional laboratory experiments [Ianzini and Mackey, 1997; Ianzini and Mackey, 1998; reviewed by Ianzini and Mackey, 2007]. The event analysis program is used to describe the yield of normal and abnormal division types, cell fusions, and cell death, and to detect patterns of reductive division and depolyploidization in cells undergoing radiation-induced MC. Additionally, the biochemical and molecular data used in conjunction with live cell imaging data are presented to illustrate the usefulness of combining biology and engineering techniques to elucidate pathways involved in cell survival under different detrimental cell conditions. In the second project, the use of long-term fluorescence live cell imaging is explored through measurements of cell division and cell death during repeated exposures to blue fluorescence excitation light. These measurements also take advantage of the event analysis program and demonstrate the usefulness of this program for describing any type of event associated with cell toxicity.

<u>Research Purpose</u>

Event Analysis in Live Cell Digital Image Sequences

Traditional biochemical and molecular measurements used to study cellular processes include assays such as PCR, RT-PCR, blotting techniques, immuno-fluorescence, and flow cytometry. Each of these techniques allow for the observation of

cell morphology or quantitative measurement of intracellular macromolecules. While these assays are important and have been utilized for many years to elucidate cellular processes, they are limited by the fact that they are static measurements. To make any of these measurements the cell sample is sacrificed therefore the results represent only a moment in time for one cell or group of cells. In contrast, live cell imaging can capture the dynamic responses of cell cultures to stimuli or damaging agents by observing the changes in morphology in a single cell. Moreover, because our live cell imaging system is non-perturbing, we can image cell populations for weeks allowing reliable measurement of cell generation length, cell death, and cell division. In addition, using fluorescence live cell imaging techniques we can detect intracellular proteins, molecules, and cell organelles. Live cell imaging certainly cannot replace traditional assays, but the combined use of it with biochemical and molecular measurements represents a powerful tool to connect dynamic observations at the cellular level to static observations at the sub-cellular level.

Due to the enormous amount of observable data in digital image sequences of living cells, we created a method to catalog and describe all of the events captured during the imaging process [Kosmacek *et al*., 2009, submitted] (Chapter 2). Events are manually detected in streaming digital images and analysis programs are used to statistically describe the yield of events and to search the data for patterns of events. The program is demonstrated here through its application to two projects in the field of cancer research: MC and fluorescence live cell imaging of cancer cells.

<center>Event Analysis of Mitotic Catastrophe</center>

Live cell imaging played a pivotal role in the first descriptions of MC and the events which lead to the formation of large, multinucleated cells after cellular insult to cancer cell populations. While cell fusion and the formation of large cells had been observed through traditional methods, live cell imaging allowed us not only to observe

the timing and kinetics of these processes but also to quantify each and every observed event. Using the event analysis program we can measure the yield of abnormal divisions, fusions, and death of cells that have undergone MC. Additionally we can use a subgraph isomorphism algorithm (described later) to detect patterns of events associated with depolyploidization of MC cells. The ability to detect subgraphs is a powerful tool for discovery of these rare event patterns in very large data sets. Without this technology it would take days or weeks for a person to examine all of the image sequences each time a new event pattern is of interest.

Molecular Mechanisms of Depolyploidization in Mitotic

Catastrophe Cells

It was observed that cells that undergo radiation-induced MC were capable of multipolar type divisions. And further, in rare instances those multipolar divisions produce mononucleated cells which resume a normal division pattern. Two questions are in order to fully appreciate these events; first, what is/are the mechanism(s) by which cells undergoing MC can successfully divide through depolyploidization? And second, what is the fate of the progeny originated from an MC cell? It is important to address both of these issues as the knowledge of the molecular pathways elicited by MC cells to escape death might be exploited for cancer treatment purposes. Moreover, by understanding the ultimate fate of the surviving cells originated from MC cells, we will find insight into cancer progression.

The reduction in DNA content and in the number of nuclei in MC cells that successfully divide has led us to hypothesize that alternative pathways of cell division other than mitosis (the division somatic cells use to produce two identical daughter cells), might be elicited under these conditions. In general, reductive division is synonymous with meiosis (the division germ cells use to produce four gamete cells with half the DNA as the parent cell). We saw a potential link between DNA content reduction in MC cells

and meiotic division. From this observation we formulated the hypothesis that meiosis-specific genes are expressed in MC cells during depolyploidization. We began testing our hypothesis by designing experiments to measure the expression of a set of meiosis-specific genes in our irradiated cell populations. Exploring the activation of these alternative pathways of division might aid in understanding the molecular mechanisms of cellular resistance to radiation treatment and offer opportunity to apply this knowledge in the cancer treatment clinical setting.

<div align="center">Measuring Fluorescence Excitation Light Toxicity in</div>

<div align="center">Living Cells</div>

In recent years the development of tools and protocols to study cellular processes with imaging has focused on the use of fluorescence microscopy [Rieder CL and Khodjakov, 2003; Conrad *et al*., 2004] which is limited by cytotoxicity from both fluorescent probes and excitation light [Kosmacek *et. al.*, manuscript in preparation]. As the technologies for live cell imaging continue to expand, researchers can now detect fluorescently labeled proteins, intracellular molecules, and organelles in living cells to further elucidate cellular processes. It is well known that fluorescent light can have toxic effects on cells [Wang and Nixon, 1978; Bradley and Sharkey, 1977; Hockberger *et al*., 1999], but the conditions that promote toxicity are not well understood. Reduction or delay of the phototoxic effects of fluorescence excitation light can be achieved by using UV filters, neutral density filters, and longer excitation wavelengths. We have implemented the event analysis software as a novel tool to detect the cellular response to fluorescence excitation light by accounting for changes in cell division and cell death. The results presented in Chapter 4 demonstrate the effect of fluorescence excitation light-induced toxicity as it is measured through event analysis and morphological observations. Using a variety of cell lines and parameters for image acquisition we provide preliminary

results that are intriguing and call for further investigation into the development of fluorescence imaging techniques for living cells.
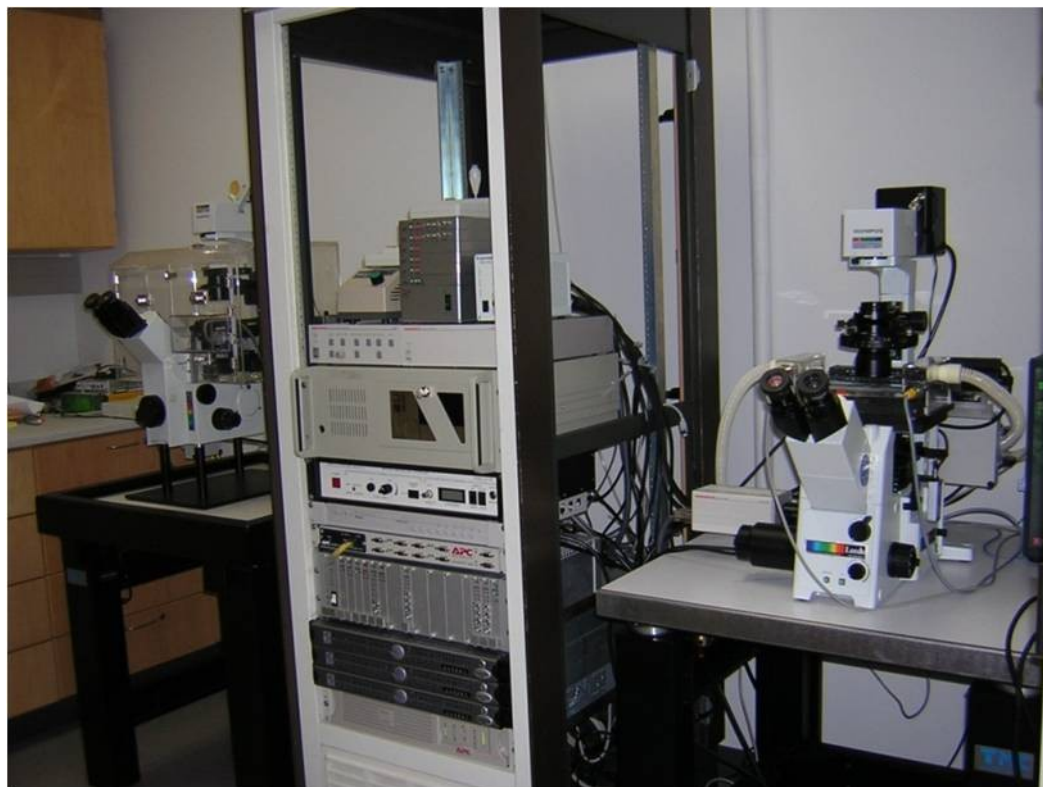
Figure 1.1: The Large Scale Digital Cell Analysis System (LSDCAS) Located in the Holden Comprehensive Cancer Center at the University of Iowa. LSDCAS is a core facility for live cell imaging that offers non-perturbing measurements for cell growth, cell death, cell motion, and fluorescence. The acquisition and storage of image data is completely automated through computer programs designed in house. Unperturbed cell growth is accomplished through the control of humidity, temperature, and $CO_2$ in the incubation chamber located on the microscope stage.

CHAPTER 2

EVENT ANALYSIS OF LIVE CELLS IN DIGITAL IMAGE SEQUENCES

Live Cell Imaging: Improved Measurements of Cell

Response to Radiation Treatment

Early digital image sequences made with the LSDCAS were used to investigate the response of HeLa cells treated with ionizing radiation as it pertained to the production of large, multinucleated cells. By streaming digital images collected every five minutes, it was observed that some of the multinucleated cells attempt multiple rounds of division before death. Further, when the division successfully produced daughter cells, the abnormal morphology of the parent cell often propagated through the generations resulting in short lived colonies of mixed morphology and a delayed death response [Ianzini and Mackey, 2002]. These observations unveiled the weakness of traditional clonogenic assays which measure the mitotic potential of a cell population. During a clonogenic assay, cells are treated, detached from the flask, counted, and then plated at low density on culture dishes. The cells are allowed to proliferate for 7-10 days; those cells that are clonogenic will divide several times and produce visible colonies. After the growth period the colonies are fixed, stained, and then counted. Not every cell plated will attach and proliferate so a control sample is always run in parallel to determine the plating efficiency of the cell culture. The equation used to calculate plating efficiency is as follows:

$$Plating\ Efficiency = \frac{Observed\ colonies\ in\ control}{Number\ of\ cells\ plated}$$

Using the observed colony counts and the known number of cells plated *per* dish, the surviving fraction of cells in the treated sample is then calculated using the following equation:

$$Surviving\ Fraction = \frac{Observed\ colonies\ in\ treated}{Number\ of\ cells\ plated \times Plating\ Efficiency}$$

Figure 2.1 illustrates the results that may be obtained from a survival assay using high and low energy radiation to treat a cancer cell population. The mathematical fitting of the data and interpretation of curve shape is a much debated topic but in general two types of curves can be generated and their shape is dependent on the mechanism of cell killing. In terms of radiation, high linear energy transfer (LET) radiation will generate a linear dose-response for cell killing, that is, exponential reduction in survival with respect to increasing dose. These types of curves are well-understood as high LET radiation at any used dose obliterates intracellular macromolecules, damages cell membrane proteins, and creates double stranded DNA breaks. In contrast, low LET radiation will produce a "curved" fit; a region at low doses that does not inactivate cell division (the shoulder) and a region at high doses which becomes nearly linear. The shoulder region is possibly the most controversial phenomenon in radiobiology; but the linear-quadratic model presented in Figure 2.1 assumes that a cell can die in two ways, through a single lethal event or through the accumulation of sub-lethal events. However, without knowledge concerning the condition of cells within the colonies, the survival fraction obtained as discussed above is simply a cumulative death count from the time of treatment to the time of fixation. In fact, the results of a clonogenic assay provide no information about the type or success of division events which produce the observed colonies, nor does it account for different types of cell death or for a mixed cell population. Additionally, the equation for surviving fraction assumes that each colony originates from a single surviving cell, leaving a large margin for manual errors during cell suspension and cell plating. Conversely, live cell imaging allows a researcher to observe the origin and fate of living cells, examine the dynamic changes in morphology as a cell progresses through its reproductive life cycle, and can produce the end information on survival capability as the clonogenic assay. For these reasons, LSDCAS is much more powerful and produces more data than traditional methods generate, and does all this without sacrificing the cells.

Imaging the Cell Cycle

LSDCAS generates a large amount of digital image data, on the order of terabytes, but more important is the content of the digital image sequences.   A majority of adherent cell lines are excellent candidates for live cell imaging, primarily determined by the quality of the cell's borders when in contact with other cells and overall transparency of the cytoplasm.  As cells move through their reproductive life cycle, they exhibit definable geometric and optical changes which are all detectable by the human eye.  Live cell imaging can capture a cell's progression through its life cycle as demonstrated in Figure 2.2.  The cell cycle is divided into four stages: G1, S, G2, and mitosis.  The first three stages G1, S, and G2 are collectively termed interphase; during this time the cell synthesizes new proteins, replicates its DNA, and metabolizes food to obtain energy and raw materials for macromolecular biosynthesis.  In streaming digital images of living cells interphase is characterized by cell growth, visible internal structures such as the nucleus, darkened borders, irregular shape, and some degree of motility.  The three stages of interphase cannot be visibly distinguished from one another, this requires measuring the DNA content of the cell; G2 cells have twice the DNA content of cells in G1 because DNA replication is completed during S-phase. Mitosis is the time a cell spends organizing then dividing its DNA into two nuclei and is comprised of four main stages; prophase, metaphase, anaphase, and telophase.  During prophase DNA condenses into chromosomes, the mitotic spindles are assembled in the cytoplasm, and the nuclear membrane breaks down.  At metaphase the chromosomes migrate to the center of the cell, aided by their attachment to the mitotic spindles via kinetichore fibers, and align to form the metaphase plate equidistant from the two spindle poles.  During anaphase the kinetichore fibers contract and shorten to facilitate sister chromatid migration toward opposite ends of the cell.  Telophase marks the end of mitosis, nuclear membranes reform around the chromosomes at each pole and cytokinesis (division of the cytoplasm) begins.  As depicted in Figure 2.2, a cell proceeding through mitosis is

spherical resulting in optical changes visible as a decrease in cell perimeter, increased pixel intensity at the borders, and loss of refined internal structures.

## Cell Event Analysis GUI and Data Representation

### *casViewer*

In digital image sequences it is observed that most adherent cell lines exhibit the same pattern of visible morphological changes (events) throughout their cell cycle as is shown in Figure 2.2. Those events related to cell division and cell death are presented in Table 2.1, they include normal and irregular division types seen in cancer cell populations. A graphical user interface, *casViewer* (Figure 2.3) was designed to allow manual identification of events by an investigator [Davis *et al*. 2007]. The interface was developed to allow flexibility in the event set used for easy application to a large variety of experiments. To acquire digital images of living cell cultures for event analysis, cells are plated at low density in either a flask or multi-well dish which is held in place on the microscope stage. Fields of view are selected by a user and the acquisition software iterates over all fields capturing images for a set duration of time. Once all the images are captured they can be streamed at a desired rate on the *casViewer*. The viewing module is equipped with VCR-like controls for steady playback or frame-by-frame, forward and rewind modes. When an event is observed the user clicks on the x,y-coordinate of the event and selects the event type from a contextual menu. Detected events appear in the event tree display module, where a user can visually verify the connectivity of events and the event types. Additionally, the user can highlight an event in the event tree display module and go to the frame in which it occurred. The data are stored in the eXtensible Markup Langauge (XML) file format as linear lists of the identified events and multiple parameters which allow reconstruction of the data into tree structures.

Graph Theory

To facilitate the analysis of the event data, a graph-based representation was used (Figure 2.4). A graph is a mathematical model of relationships between objects where those objects are represented as nodes or vertices and are related by edges. A graph $G$ with $n$ vertices and $m$ edges has a vertex set $V(G) = \{v_1, v_2, ..., v_n\}$ and an edge set $E(G) = \{e_1, e_2, ..., e_m\}$. In a simple connected graph (Figure 2.4A) each edge, $e$, consists of two vertices, $uv$, called its endpoints such that $e = \{uv\} = \{vu\}$, and if $uv \in E(G)$ then the vertices are adjacent, or connected. A directed graph (Figure 2.4B) contains an edge set where each edge is an ordered pair of vertices, $uv$, where $u$ is the tail and $v$ is the head. A directed edge $e = \{uv\} \neq \{vu\}$ represents a uni-directional relationship from $u$ to $v$, also written as $u \rightarrow v$. A directed acyclic graph (DAG) is directed, but contains no directed cycles. In other words, for any vertex $v$ in a DAG there is no path which begins and ends on $v$ (Figure 2.4C). [West, 1996] DAGs are used for a variety of applications including phylogenetic trees in bioinformatics, statistical modeling with Bayesian networks, hierarchical file systems or databases.

DAGs are an ideal format for representing cell event data as they have a natural linear topological ordering which can be represented in a tree structure, much like that in Figure 2.4D. Each cell analyzed has a vertex set, or event set, which are uni-directionally related as parent and child events. Every set of events has a root, or source, event which has no incoming edges and identifies the cell to be analyzed in the first image (frame). Also, each event set has several leaves, or sinks, which can be cell death, movement of the cell off-screen, or indication that the analysis was terminated while the cell was alive. These terminating events never have an outgoing edge and can be used in conjunction with the root event to partially validate the quality of data prior to analysis. Each event node contains several pieces of data, including the event name, the time it occurred, the field and frame number of the digital image sequence, the x,y-coordinates of the event within the field of view, the event id which is unique to the experiment, and the event id

of all parent events. The natural ordering of events is related to their occurrence in time, so an event at a later time never points to one that took place before it, hence the data is always acyclic. An example of a cell event DAG is shown in Figure 2.5, this DAG was constructed from event data detected in a non-treated HeLa Clone3 cell.

<u>Subgraph Isomorphisms in Cell Event Trees</u>

The use of labeled DAGs to represent the events provides for a unique method to complete data mining. A graph $G$ can be defined by a user and then compared to an experimental event tree $H$ to determine if graph $H$ contains a subgraph isomorphic to $G$. In this way, we can define patterns of events that are of interest and determine the frequency with which our data set contains that pattern. This problem of finding a subgraph within a larger graph is known as the subgraph isomorphism problem and is classified as having solutions of n-polynomial complexity. While some solutions to this problem provide a measure of similarity for two graphs [Levi, 1972], we require an algorithm to return exact subgraph isomorphisms for a given query graph. General methods for solving the subgraph isomorphism problem have utilized backtracking algorithms [McGregor,1982]. Optimizations to improve backtracking have been described by Ullman [Ullman, 1976] and include checking the isomorphism during recursion and abandoning search paths as early as possible. Ullman's algorithm was further improved [Krissnel and Henrick, 2004] to include a forward looking function that determines the validity of a search path as well as ignoring branches that don't have the required depth to satisfy the query graph. Checking for graph depths improves the performance of the algorithm as the size of the query graph grows.

We have developed a software package that is based on the work of Krissinel and Henrick [Krissnel and Henrick, 2004] to find exact subgraph isomorphisms in our cell event graphs. The node equality function required by the Krissinel algorithm is implemented as a comparison of node types, thus two nodes match if their types match.

The edge equality function is implemented by evaluating the node comparison function for both pairs of corresponding nodes. An example of a queried DAG from a normally dividing cell is shown in Figure 2.6. In this instance the query graph defines a normal division event, followed by a flatten out event, then a round up event, and finally another normal division. This query represents a series of events typical to normally dividing cells and would match to two subgraphs within the given DAG. Measurement of the time interval between normal division events provides insight to the condition of the imaged cell population. The timestamps returned can be used to estimate the average doubling time for the population. In addition, we store a generation number which allows us to easily segregate the generations for doubling time analysis. This allows us to determine if an early delay is propagated in multiple rounds of division after treatment. We can also estimate the time spent in mitosis as the time from the cell round up event to the time a division event is labeled.

An extension to the algorithm was implemented to allow for wildcard matching between nodes and edges to allow for querying underspecified graphs. Matching wildcard node types is a straightforward addition by extending our node comparison function to match a special label against any node type. Specifying events that can be an arbitrary distance apart involves breaking the wildcard edge and then checking returned subgraphs for compatibility with the edge distance specified. These features are advantageous if a particular event and downstream outcome are of interest, but the intervening events are unknown or unimportant. If the objective is to determine unknown event patterns, wildcard queries can be utilized to identify partial matches and the returned subgraphs examined to refine the query.

<div align="center">Individual Event Yield Analysis</div>

Using the data collected with *casViewer,* we have designed programs to quantify the yield of individual events or categories of events with respect to time. These analysis

programs can accommodate arbitrary event type definitions by relying on specified event attributes. Those attributes include; a cell count modifier, generation number modifier, pointers to other event trees within the same experiment, definition as a root event, definition as a terminating event, and expected number of relationships to or from the event. To measure the yield of an event we calculate the frequency of each event or event category *per* cell being analyzed and accumulate those frequencies over the course of the entire experiment. The number of cells being observed at any given time N(t) is determined by the following equation:

$$N(t) = \sum_t IC + \sum_t ND + \sum_t (MD \mid FMD-> FO-1) - \sum_t SCF - \sum_t \frac{NSCF}{2} - \sum_t OS$$
$$- \sum_t DD - \sum_t DT - \sum_t ID - \sum_t EOA$$

Events are then binned into appropriate time intervals, we generally use 3-8 hour bins, and the yield of an event up to a given time is then described by the equation:

$$Y(event) = \sum_t \frac{frequency(event)/bin}{Cell\ count/bin}$$

To implement these calculations, computer programs for the analysis were written in C++ and with Perl scripts. First, we read in every event contained in the xml files for a single experiment and sort them according to their timestamps. Next we process the event's cell count modifiers as shown in Table 2.2. Cell count increases when cells are identified or when division events occur. Cell count decreases when cells fuse, die, or move off screen. Special conditions include multipolar divisions and non sister cell fusions. Division events defined as capable of producing more than two daughter cells are assigned a cell count modifier that is one less than the number of relationships leaving that event node. For the case of non-sister cell fusions if both cells were being tracked the events must be merged, subtracting one from the total number of cells observed. After cell count is calculated the events are sorted into bins and the frequency of the

event *per* bin is normalized to the number of cells at the bin start time. The instantaneous and accumulated frequencies, or yield, of events *per* cell are written to a text file for plotting in any graphing program.

## Validation

Validation included verification of raw data in the event counts both for a single event and for queries of event connectivity, mathematical calculation of cell number and event yields, and by visual inspection of the image sequences to determine if the output realistically represents the effects of treatment. The validation of results output by the software was conducted using digital image sequences of cells undergoing MC. The events presented in Table 2.1 were designed for identification of events related to MC, and are therefore all present in those experiments. Using MC data sets ensured that all event types and relationships could be detected and properly analyzed. This included merging of symmetrical event relationships such as with normal divisions and fusions, as well as multiple parent to child relationships as found in multipolar division types. The events, identified using *casViewer* interface, were also manually entered into spreadsheets to provide a comparison for the data output by the analysis software. Manual analysis and mathematical calculations verified the algorithm's internal consistency. However, the raw data showed inconsistency through the expected cell counts. In theory, if all cell event DAGs are processed from the beginning to the end of the experiment's duration, the cell count should go to zero. When the cell count was examined, the output often contained numbers greater than zero. This could have been a result of lost data or data that was missing from the DAGs. It was confirmed that the program was successfully reading in every event, so the DAGs themselves were examined. The source of error proved to be at the user level, where fields of view were incompletely analyzed, incorrectly identified, and incorrectly connected. As it is difficult to eliminate human error at the source, we defined specific event attributes (Table 2.2)

and designed programs to scan the event trees for discontinuities in event attributes. The program then generates error messages prompting the user to return to a particular field and event number with a brief description of the error. With human error essentially eliminated from our raw data we are confident that the analysis programs are accurately measuring event yields and detecting subgraphs.

Dose dependant probability of survival after irradiation
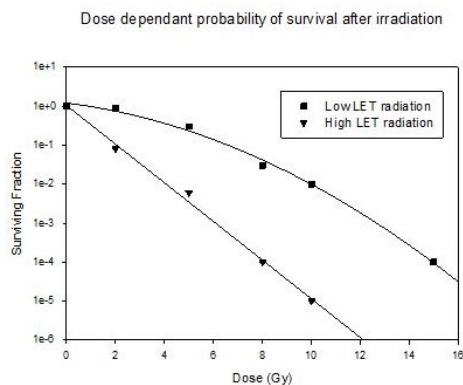
High LET radiation curve

$Surviving\ Fraction = e^{-\alpha D}$ , where $\alpha$ is the slope of the curve and D is the dose

Low LET radiation curve

$Surviving\ Fraction = e^{-(\alpha D - \beta D^2)}$ , where $\alpha$ and $\beta$ are constant and D is the dose

Figure 2.1: Cell survival data is generally displayed on a semi-log graph of surviving fraction versus treatment or time after treatment. In this example the surviving fraction of cells is reported with respect to the dose of radiation received. The commonly used curve fitting models for high and low LET radiation are shown on the right. The interpretations of these results are still debated but often include reference to cell repair mechanisms or target theory.

Late Interphase (S/G2) – Cell is spread out over flask surface, internal structure is visible. Cell has grown to its largest size before mitosis.

Metaphase – Chromosomes are aligned at metaphase plate, cell is round and borders are bright

Anaphase/Early Telophase – Chromosomes have migrated to opposite poles, nuclear envelope may be reforming but cytokinesis is not evident yet.

Late Telophase/Cytokinesis – Cytoplasmic division is complete or nearly complete, two daughter cells are visible

Early Interphase (G1) – Cells are flattening out over surface and growing in size, internal structure is becoming visible.

Figure 2.2: A single cell's progression through its life cycle can be observed in streaming digital images. Morphological and optical changes in the cell can be used to determine the approximate location in the cell cycle. Red arrows are used to indicate the condensed chromosomes visible in metaphase and anaphase/early telophase. Condensed chromosomes are not always visible in the images as the mitotic cell is spherical and the plane of focus will not necessarily fall into the same z-coordinate as these structures. Late interphase and early interphase were determined based on their close timing to the beginning and end of mitosis.

| Event Notation | Full Event Name | Description |
|---|---|---|
| IC | Identify Cell | Mononucleated cell at frame 0 |
| ICBN | Identify Bi-nucleated Cell | Bi-nucleated cell at frame 0 |
| ICMN | Identify Multinucleated Cell | Multinucleated cell at frame 0 |
| RU | Round Up | Cell has become round and is at or near smallest diameter, internal structures are rarely visible |
| ND | Normal Division | Parent cell successfully divides into two daughter cells |
| FND | Failed Normal Division | Parent cell attempts to divide into two cells, but produces only one daughter |
| MD | Multipolar Division | Parent divides into more than two cells, mitotic poles attempted equal daughters produced |
| FMD | Failed Multipolar Division | Cell attempts to divide into more than two cells, mitotic poles attempted are greater than daughters produced |
| FO | Flatten Out | Rounded cell is spread out and internal structures become visible |
| FOBN | Flatten Out – Bi-nucleated | Cell is spread out and internal structures become visible, cell has two nuclei |
| FOMN | Flatten Out – Multinucleated | Cell is spread out and internal structures become visible, cell has more than two nuclei |
| SCF | Sister Cell Fusion | Two daughter cells fuse after a division event |
| NSCF | Non-sister Cell Fusion | Two unrelated cells fuse |
| DD | Death at Division | Cell death while rounded up but before division |
| ID | Interphase Death | Cell death during interphase, cell is flattened out |
| DT | Death at Telophase | Cell death after division, cell is rounded |
| AP | Apoptosis | Cell death during interphase; shrinking, blebbing, and nuclear breakdown occur |
| NF | Nuclear Fusion | Nuclei or nuclear fragments fuse during interphase |
| EOM/EOA | End of Movie/Analysis | Cell is alive and the final frame has been reached or analysis was terminated due to confluency. |
| OS | Off Screen | Cell crosses the boundary of the field of view |

Table 2.1: **Visibly detectable events related to cell death and cell division.**

The events shown in this table have been used in the applications discussed here. This table provides the full name of the event, the shorthand notation, and a brief description. The software is not limited to the events presented in this table, additional events or an entirely new event set can be generated by the user to fit a particular project's requirements.
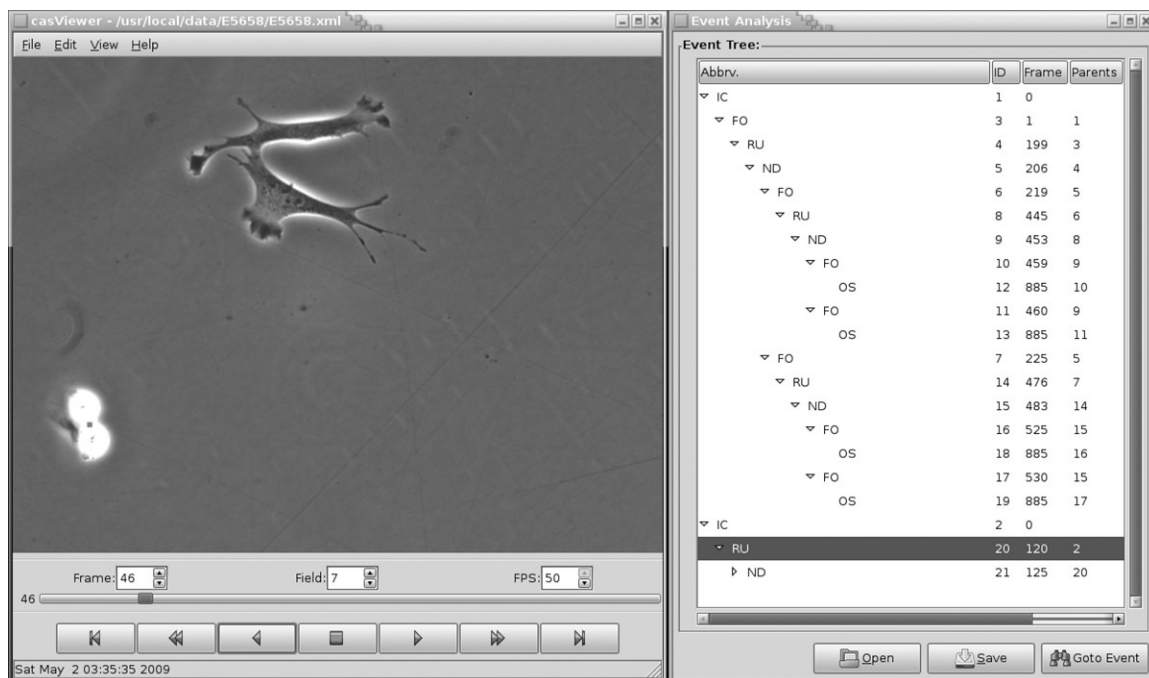
Figure 2.3: *casViewer* consists of a movie player (left) with continuous or frame-by-frame options for viewing a movie. To the right of the viewer is the event tree display module. As a user identifies new events they are added beneath any highlighted events in the tree.
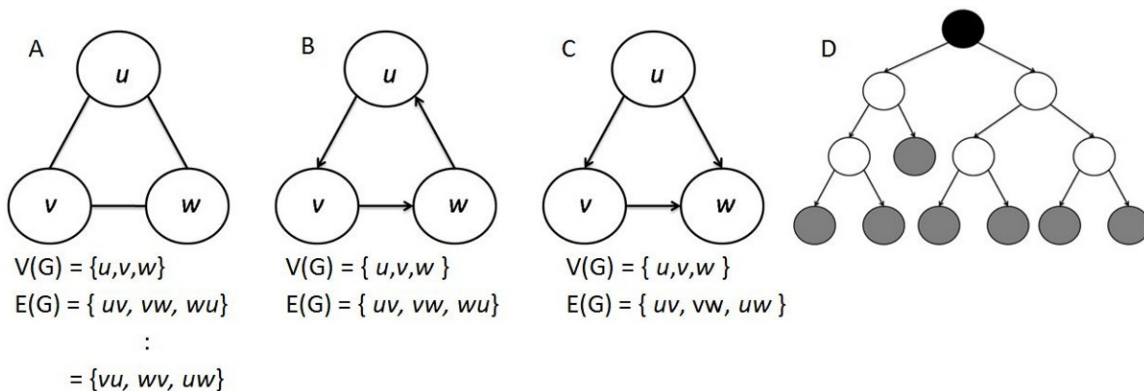
Figure 2.4: A graph G is described by a vertex set, V(G) and an edge set, E(G). [A] A simple, connected graph has many possible edge sets which describe the relationship between vertices. [B] A directed graph has one vertex set and edge set. This contains a directed cycle, starting a path from any vertex will end on the same vertex. (For example A → B → C → A) [C] A directed, acyclic graph (DAG) has directed relationships between vertices, but contains no directed cycles. [D] DAGs are commonly used in models where a hierarchical ordering of vertices results in a tree structure. At least, one vertex has no incoming edges called the root (black) and several vertices have no outgoing edges called sinks (grey).
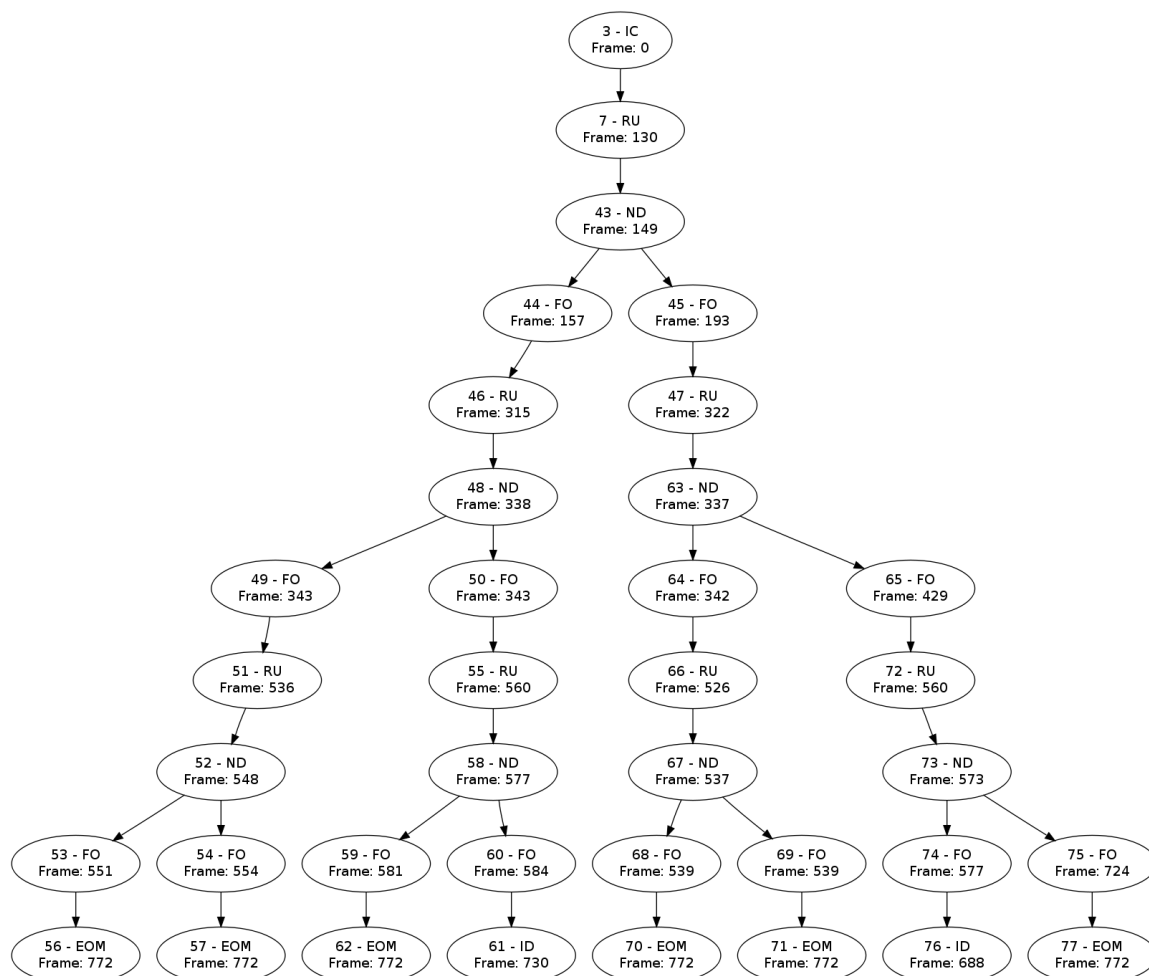
Figure 2.5: A DAG produced by analysis of a HeLaClone3 cell growing normally. This event tree shows the typical sequence of events from control cell populations. Whenever the cell event trees are queried for a particular pattern these graphical representations of the data can be generated for visual verification of the matching subgraphs.
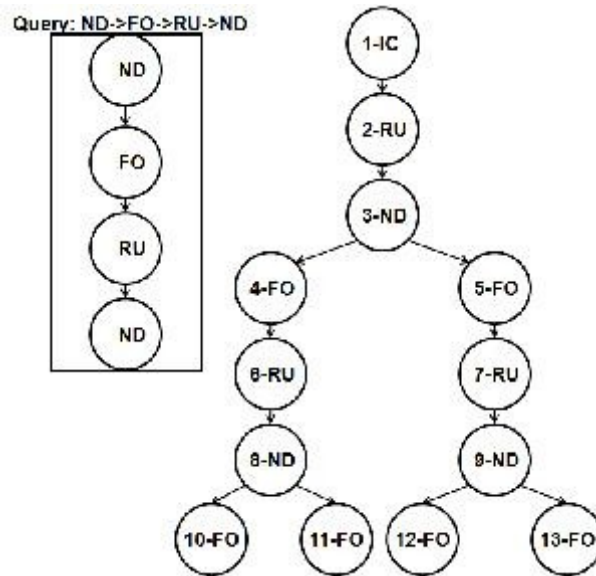
Figure 2.6: Subgraph isomorphisms are used to detect a particular pattern of events. An example of a DAG produced by a cell undergoing two rounds of normal division. The query defines a graph that begins with a normal division (ND) producing a mononucleated daughter (FO) which rounds up (RU) and divides normally again (ND). This event tree contains two matching subgraphs to the query, 3→4→6→8 and 3→5→7→9.

| Event Notation | Cell Count Modifier | Generation Modifier | Root/Leaf | Incoming(in)/Outgoing(out) Relationships Expected |
|---|---|---|---|---|
| IC | 1 | 0 | Root | 0 in / 1 out |
| ICBN | 1 | 0 | Root | 0 in / 1 out |
| ICMN | 1 | 0 | Root | 0 in / 1 out |
| RU | 0 | 0 | Neither | 1 in / 1 out |
| ND | 1 | 1 | Neither | 1 in / 2 out |
| FND | 0 | 1 | Neither | 1 in / 1 out |
| MD | #Daughter cells - 1 | 1 | Neither | 1 in / >2 out |
| FMD | #Daughter cells - 1 | 1 | Neither | 1 in / ≥1 out |
| FO | 0 | 0 | Neither | 1 in / 1 out |
| FOBN | 0 | 0 | Neither | 1 in / 1 out |
| FOMN | 0 | 0 | Neither | 1 in / 1 out |
| SCF | -1 | 0 | Neither | 2 in / 1 out |
| NSCF | -1 | Use greater gen # | Neither | 1-2 in / 1 out |
| DD | -1 | 0 | Leaf | 1 in / 0 out |
| ID | -1 | 0 | Leaf | 1 in / 0 out |
| DT | -1 | 0 | Leaf | 1 in / 0 out |
| AP | -1 | 0 | Leaf | 1 in / 0 out |
| NF | 0 | 0 | Neither | 1 in / 1 out |
| EOM/EOA | -1 | 0 | Leaf | 1 in / 0 out |
| OS | -1 | 0 | Leaf | 1 in / 0 out |

Table 2.2: **Event attributes used by the analysis and validation programs.**

The events shown in this table have been used in the applications discussed here. This table provides the event attributes values required for cell count and generation calculation or for raw event validation and error reports. Event attributes are another robust aspect of the event analysis design, allowing easy incorporation of new events to be detected and measured. For full event name or event definitions refer to Table 2.1.

CHAPTER 3

MITOTIC CATASTROPHE IN IRRADIATED CANCER CELL POPULATIONS

Mitotic Regulation and Cancer

The cell life cycle is controlled by regulatory proteins, cyclin dependent kinases (cdk), which obtain substrate specificity when in complex with proteins called cyclins. The cyclin-cdk complex activity oscillates within the cycle, resulting in properly timed phosphorylation of intracellular proteins to initiate major events such as DNA replication and mitosis. The normal progression from G2 phase to M phase is primarily facilitated by Cyclin B1/cdc2 (where cdc2 is cdk) complexes which are active in varying phosphorylation states. The Cyclin B1/cdc2 complex is inactive during S and most of G2 phases through phosphorylation of cdc2 at Thr14 and Tyr15 by wee-1 kinase. Conversely, the complex is activated at the very end of G2 phase through phosphatase activity of Cdc25C which removes inhibitory phosphate groups on Cdc2 promoting complex translocation to the nucleus. Once inside the nucleus the CyclinB1/cdc2 complex phosphorylates structural and regulatory proteins inducing the assembly of the mitotic spindle, breakdown of the nuclear membrane, and attachment of the chromosomes to the spindle apparatus. Following entry into mitosis the cell begins degrading the Cyclin B1/cdc2 complex through first Gadd45 mediated dissociation of the complex followed by proteosomal degradation of the proteins [Pines and Hunter, 1991].

If a cell has accumulated macromolecular damage, especially DNA damage, pathways can be triggered to halt the cell cycle progression and allow the cell to repair itself or initiate death pathways. There are many genes and pathways involved in cell cycle arrest at various checkpoints in the cell cycle, discussed here is one general pathway for arrest at the late G2/M checkpoint. One important regulator of cell cycle following damage is the p53 gene which functions through transcriptional regulation of downstream genes that arrest cycling cells. Although p53 is not required to initially arrest

a cell at the G2/M checkpoint, it is required to maintain the arrest while the cell repairs its damaged DNA. [Reviewed by Vogelstein and Kinzler, 1992] In response to damage the p53 protein becomes activated and up-regulates transcription of inhibitory genes such as p21, GADD45, chk1, chk2, and 14-3-3-σ. p21 can bind to and inactivate cdc2 directly while chk1, chk2, and 14-3-3-σ all initiate pathways to inhibit Cdc25C activity and prevent translocation of the Cyclin B1/cdc2 complex to the nucleus. In addition to promoting complex dissociation via GADD45, p53 can also directly down-regulate the transcription of Cyclin B1 and cdc2 [reviewed in Taylor and Stark, 2001].

The p53 gene is especially important when studying cancer cells, because over fifty percent of solid tumors have non-functional p53 protein. Damaged cancer cells which lack functional p53 can over-accumulate CyclinB1/cdc2 complexes and do not arrest or only briefly arrest in response to DNA damage. The loss of checkpoint control does not allow for proper repair of DNA and sometimes results in the cell's premature entry into mitosis. These findings have been used to enhance tumor killing via radiation therapy by taking advantage of the cells' inability to repair themselves after being damaged. However, these forms of cancer therapy can result in the regrowth of tumors with increased resistance to the treatment, suggesting the mechanism that allows for mass cell killing may confer a selective survival advantage in a small percentage of cells.

<div align="center">Mitotic Catastrophe</div>

Mitotic catastrophe (MC) is a cellular phenomenon in which rounds of abnormal or aborted mitoses result in cell fusion shortly after cytokinesis or failure to complete cytokinesis and produces large, multinucleated cell progeny [Ianzini and Mackey 1997, Ianzini et al. 2006]. MC has been studied since the late 1980's, its discovery was connected to research of cell cycle regulators, including wee-1 and Cdc25C, as well as abnormal mitotic events following cellular insult [Russel and Nurse 1987, Mackey et al. 1988, Molz et al. 1989]. These early studies noted that several days after cellular stress,

such as mild heat or radiation treatments, there appeared a sub-population of giant cells within the cell culture which were aneuploid or polyploid.  Morphologically MC cells are much larger than their control counterparts, are multinucleated with intact nuclear membranes (termed sub-nuclei), and have a disorganized arrangement of intracellular organelles.   The generation of these abnormal cells is preceded by accumulation of pro-mitotic proteins such as CyclinB1, abrogation of cell cycle checkpoints, and subsequent early entry into mitosis.  The occurrence of MC correlates to the p53 status of a cell line, and is observed at a much greater degree in those cells which do not have a functional p53 protein.  It has been proposed that MC may be used by the cells deficient in apoptotic pathway as an alternative mode of death [Mackey and Ianzini 2000, Ianzini *et al.* 2007] [reviewed in Castedo 2004 and Ianzini and Mackey book chapter 2007].  The early biochemical and imaging data regarding cells undergoing MC indicated that nearly all of these cells would eventually die but a very small percentage showed at least a limited potential for survival [Ianzini and Mackey, 2002].

Streaming digital images have shown that MC cells are capable of abnormal divisions and sometimes these divisions produce single nucleated progeny [Ianzini *et al*., 2009].  Interestingly, DNA image cytometry results suggest that later generations of MC cells have less DNA content *per* sub-nuclei than is present in cells soon after the initial MC event; that is, MC cells undergo depolyploidization [Erenpreisa *et al*., 2005].  These data suggest that reorganization and reduction of DNA is a path which MC cells, that are able to escape death, seem to activate possibly to gain genetic stability making them prone to overall survival.  The events associated with reductive division are interesting because in nature reductive divisions occur in gametes and germ cells through a specialized division process, meiosis.  In addition to reducing DNA content, the purpose of meiosis is to reorganize and exchange genetic information thereby maintaining genetic diversity in a population.  In the cases that we are studying, when a multinucleated cell gives rise (among others) to a smaller cell with a single nucleus, in fact reducing its DNA

content, the question of if this reduction is favored by meiotic pathways becomes permissible. In the studies discussed later of radiation induced MC and of escape of MC cells from death, we will see that specific meiotic genes are activated during the depolyploidization events observed with live cell imaging techniques.

<p style="text-align:center">Meiosis</p>

During meiosis a diploid mother cell completes two divisions after only one round of DNA replication, producing four haploid daughter cells. Each meiotic division has a prophase, metaphase, anaphase, and telophase which are differentiated by a *I* in the first division and a *II* in the second division. Meiosis I results in the pairing of homologous chromosomes, genetic recombination, and finally separation of homologs into the daughter cells. Prophase I takes up the majority of the time required for meiosis and is divided into five stages; leptotene, zygotene, pachytene, diplotene, and diakinesis. In leptotene stage, homologous chromosomes pair and sister chromatids condense, unlike mitosis the nuclear envelope remains intact throughout prophase I. During zygotene a ladder-like protein structure, known as the synaptonemal complex (SC), begins to form between homologs and the synapsis is complete before pachytene stage. Pachytene stage begins the genetic exchange process in which double strand breaks are created in the DNA and crossover events occur. Diplotene stage is the period of desynapsis when the SC breaks down and chiasmata become visible at the points of DNA stand exchange between homologs. The persistence of the chiasmata after SC breakdown has been suggested to play a role in proper alignment of homologs at the equatorial plate during metaphase and failure to align homologs results in aneuploid progeny [Hassold and Hunt, 2001]. During the final stage of prophase I, diakinesis, the nuclear envelope breaks down, the spindle apparatus forms, and chromosomes condense further in preparation for division. At metaphase I the homologous chromosome pairs align along the equatorial plate as spindle fibers elongate and attach to the centromeres. As anaphase I proceeds,

sister chromatids remain together but homologous pairs are pulled toward opposite poles as spindle fibers contract and shorten. Finally, during telophase I, nuclear envelopes reform around the separate sets of homologous chromosomes, chromatin decondenses, and cytokinesis proceeds. Meiosis I is followed by interkinesis, an interphase-like period of growth where DNA is not replicated. Meiosis II is analogous to mitosis although there is only one copy of each chromosome containing two sister chromatids and the progeny are haploid daughter cells.

A set of specific genes tightly regulate the process of meiosis I where homologous chromosomes are paired, genetic material is exchanged, and recombination occurs. The following is a brief discussion of the meiosis-specific genes that, for their involvement in genetic material organization and recombination, we have decided to analyze in order to test the hypothesis presented above. One important aspect of meiosis I is the pairing of homologs to facilitate both DNA exchange and proper segregation of the chromosomes so that each daughter cell contains a full copy of the genome. One important component of chromosome pairing is the SC, a ladder structure composed of three proteins (SYCP1, SYCP2, and SYCP3) which interact to form a central element that connects two lateral elements. During leptotene stage cohesin complexes (which include the meiosis-specific proteins REC8 and STAG3) associate with the chromosomes and are stabilized by SYCP2 and SYCP3 along the axis of the chromosomes to create lateral elements of the SC. Throughout zygotene stage, SYCP1 associates with proteins of the lateral elements, forming the central element and synapsis of homologs [Reviewed in Revenkova and Jessberger, 2006]. At pachytene, when synapsis is complete, the DNA topoisomerase SPO11 creates several double strand breaks along the chromosomal axis. DNA repair proteins quickly associate with the chromosomes at the sites of damage; these include but are not limited to Rad51 and associated proteins (Rad51AP2), DMC1, the breast cancer susceptibility genes BRCA1 and BRCA2, Atm/Atr (ataxia telangiectasia A-T mutated) genes, and the MMR (mis-match repair)-family of proteins. Although the process is not

completely defined in mammals, it is currently known that the recombination event is completed through double stranded break repair methods involving Holliday structure formation or synthesis dependent strand annealing. The results regarding the expression of many of these meiosis-specific genes in MC cells during depolyploidization are discussed further below.

<div style="text-align: center;">

A Mechanism For Depolyploidization of Cells That Have

Undergone Mitotic Catastrophe

</div>

The first streaming digital images depicting MC were obtained by imaging HeLa Clone3 cells, a human cervical cancer cell line that has been a model cell culture for years and of which the behavior is well understood. These cells lack functional p53 protein due to viral infection and cannot undergo apoptosis. It has been well documented in our lab that when HeLa cells are treated with damaging agents such as ionizing radiation they over-accumulate cyclin B1, abrogate cell cycle checkpoints, enter mitosis prematurely, become large and multinucleated, and display delayed DNA damage [Ianzini and Mackey 1997; Ianzini and Mackey, 1998; Mackey and Ianzini 2000; Ianzini *et al.* 2006; Ianzini *et al*. 2007]. However, time-lapse microscopy using LSDCAS reveals another important feature of these giant cells, they are reproductively active often in abnormal ways [Erenpreisa *et al*., 2008; Ianzini *et al*., 2009]. In the first 72 hours following 5Gy gamma irradiation it was observed that cells which did not die immediately would often divide normally. Following division, the daughter cells produced would fuse back together after a short period, creating bi-nucleated cells. The bi-nucleated cells have a potential to divide into more than two cells, termed a multipolar division. Following the cells for three weeks post irradiation showed that most cells attempting or completing multipolar type divisions eventually die. However a few rare instances of renewed normal divisions following multipolar divisions did occur [Ianzini *et al*., 2009]. Figure 3.1 shows still frames from the image acquisition experiment for

these events, in which a cell undergoes a fusion event then successfully completes a multipolar division to create mononucleated offspring. One of the daughter cells resumes a normal mitotic division regimen for at least two generations. These observations reinforce the hypothesis that cells may initiate pathways to reduce their ploidy and recover from potentially lethal damage induced by radiation.

## Event Yield Analysis in Cells Undergoing Mitotic
## Catastrophe

To quantitatively describe the effects of high dose gamma irradiation to cancer cell populations we utilized the event analysis program. MDA-MB435, human melanoma/breast carcinoma cells were treated with either 5Gy or 10Gy gamma irradiation, then imaged for 2 weeks post irradiation. Manual event detection was performed using the event set presented in Table 2.1. Yield analyses of these data are shown in Figure 3.2. Normal divisions (Figure 3.2A) in the control population increase exponentially with first order kinetics while the irradiated cell populations reach a plateau after a growth period of 80 h and 40 h post 5Gy and 10Gy radiation dose, respectively. The death related event analysis (Figure 3.2D) reveals that death occurs in a dose-dependent relationship where lower doses induce less cell death. These trends in cell division and cell death agree with traditional clonogenic data which have been used to document a dose-dependent reduction in cell survival after radiation treatment. The MC related events, such as multipolar divisions (Figure 3.2B) and cell fusion (Figure 3.2C) show a different trend. Interestingly, in lower doses, fusions and multipolar divisions occur over a longer period of time and at a much greater yield than is observed at higher doses. The majority of multipolar type divisions in cells receiving 5Gy radiation occur from day 2 to day 5 post-irradiation, with an additional spike around day 12. Fusions are persistent in 5Gy irradiated cells from day 2 to day 7 post irradiation.

The same type of experiment was conducted with HeLa Clone 3 cells. Yield analyses of event data collected over 12 days post-irradiation are shown in Figure 3.3. Normal divisions (Figure 3.3A) in the control population increase exponentially with first order kinetics while the irradiated cell populations reach a plateau after a growth period of 180 h and 70 h post 5Gy and 10Gy radiation dose, respectively. The death related events (Figure 3.3D) also display a dose-dependent relationship where lower doses induce less cell death and at a slower rate than is observed with higher doses As with the MDA-MB435, in lower doses, multipolar divisions (Figure 3.3B) and fusions (Figure 3.3C) occur over a longer period of time and with a greater yield than was measured after higher doses of radiation treatment. However, in the HeLa cells the yield of multipolar divisions and fusions (hallmarks of MC) are two times larger than in MDA-MB435 cells (compare Figures 3.3C and 3.3D to Figures 3.4C and 3.4D). The majority of multipolar type divisions in cells receiving 5Gy radiation occur from day 2 to day 5 post-irradiation. Fusions are persistent in 5Gy irradiated cells from day 2 to day 9 post-irradiation. These data characterize the events during and after the production of MC cells following damaging radiation treatments. We will compare the molecular and biochemical measurements (discussed further below) using the timing of events elucidated with the event analysis program to further confirm our hypothesis that MC cells successfully accomplish depolyploidization through multipolar division.

## Subgraph Isomorphisms For Event Connectivity in Cells
## Undergoing Mitotic Catastrophe

Sub-graph isomorphisms to detect patterns of normal division are used to measure generation length and this type of analysis was performed on control and irradiated cancer cell populations. Figure 3.4 shows an example of generation length distributions in MDA-MB435 cells. Statistical descriptions of generation length and mitosis length are presented in Table 3.1. Using the Mann-Whitney rank sum test we determined that the

5Gy irradiated population shows significant (p=<0.001) increases in both the time between normal divisions and the time to complete mitosis.

Additional queries were used to determine the potential of multipolar divisions to produce mononucleated cells. The data from HeLa Clone3 cells irradiated with 5Gy gamma rays were queried for multipolar division events with relationships to mononucleated flatten out events. The query (MD|FMD → FO) returned 124 subgraphs, as compared to the total number of mononucleated cells produced after divisions of any type (1402 FO events) it can be said that approximately 9% (124/1402) of the mononucleated cells arise from multipolar division types. Those 124 mononucleated cells were produced from 74 different multipolar division events, a total of 210 multipolar division events were detected, so a full 35% (74/210) of multipolar divisions produce mononucleated cells. The query was then refined to determine if the mononucleated cells produced from multipolar divisions were viable. The refined query (MD|FMD → FO →.*→EOA) matched 8 subgraphs within our HeLa Clone 3 data set. The query above utilizes the wildcard capabilities of our subgraph isomorphism algorithm (discussed in Chapter 2), and allows any type and number of events to occur from the "flatten out" event to the "end of analysis" event. To determine if any of these cells were producing normal divisions, the query was again refined to include a repeatable pattern of normal division in place of the wildcard (MD|FMD → FO → .(RU → ND → FO) → EOM). The final query returned only one match and that cell is depicted in Figure 3.1, this phenomenon while important, is difficult to detect as it occurs in less than 0.1% of all cells analyzed.

We next repeated the above set of queries on MDA-MB435 cells treated with 5Gy gamma irradiation. The first query (MD|FMD → FO) returned 71 subgraphs where multipolar divisions produced mononucleated daughter cells. A total of 971 mononucleated cells were produced by all division types, thus 7% of mononucleated cells originated from multipolar division events. Those 71 mononucleated cells were produced

from 44 different multipolar divisions which represent 43% (44/102) of all multipolar divisions observed over the two week period. The next query (MD|FMD → FO →.*→EOA) returned two subgraphs, both of which originate from the same multipolar division and are mononucleated and living at the end of the image sequence. However neither of these cells completed a normal division during the acquisition time, so their clonogenicity was not confirmed.

<p style="text-align: center;">Reduction of DNA Content</p>

To determine the extent of the radiation-induced ploidy in MC cells we used DNA image cytometry to measure the DNA content of individual sub-nuclei within the giant multinucleated MC cells. DNA image cytometry is a common technique for determining the relative DNA content within a cell population. Using slide preparations of HeLa S3 and HeLa Clone 3 cell lines and DNA cytometry techniques (Image Pro Plus 4.1) the DNA content of control and irradiated cells was measured. An example of the varied ploidy among sub-nuclei is shown in Figure 3.5.

The results in Figure 3.6 show that at 4 days post-irradiation HeLa S3 cells contain two major classes of total DNA content, 8C and 16C. Less frequently observed were populations of 6C and 12C cells. The giant cells have an average of 4 sub-nuclei *per* cell which contain from 2C to 4C DNA each. At 9 days post-irradiation the main populations have total DNA content between 4C and 8C however the sample sizes are very small. The average number of sub-nuclei remains at 4 but they have a much tighter distribution around 2C, suggesting that events have occurred to reduce the cell's DNA content at the level of the sub-nuclei.

Table 3.2 shows the comparison of other nuclear parameters from the same DNA image cytometry experiment presented in Figure 3.6; standard deviation of optical density (OD) describes texture, standard deviation of integrated optical density (IOD) measures heterogeneity in the DNA, and standard deviation of the area gives a

description of nuclear shape among the population. Collectively these data suggest that from day 4 to day 9 post-irradiation, the sub-nuclei of polyploid cells are beginning to resemble non-treated cells by becoming more evenly shaped, textured, and less heterogeneous in DNA content. These results parallel the imaging data (discussed above) that show by this same time MC cells undergo multipolar divisions.

## Morphological Studies

Morphological studies, performed in parallel with the nuclear image cytometry show a high instance of large multinucleated cells early and a repopulation of smaller mononucleated cells by 20 days post-irradiation. Some images contained multinucleated cells that appeared to be dividing and producing mononucleated daughter cells. In addition, we observed features that resembled SCs among condensed DNA as seen in Figure 3.7A. SCs (as described earlier) are a hallmark of the late zygotene/pachytene stages of meiosis I, during this timeframe sister chromatids pair and exchange DNA to naturally maintain variance in a population. We noted that many of the multinucleated cells contained thin strands of DNA that ran between the sub-nuclei, an example is shown in Figure 3.7B. These same features have also been observed in streaming digital images of MC cells. It is possible that these DNA strands play a role in cell fusion or failed mitoses. These observations collectively support the hypothesis that MC cells are capable of reducing their DNA content and that meiotic pathways might be involved in this reduction. Molecular analysis performed on MC cells should provide insights into the potential activation of these meiotic pathways.

## Meiotic Gene Expression

To confirm the cytological data that pointed towards the presence of meiotic features in MC cells, we utilized molecular biology techniques such as quantitative reverse transcription polymerase chain reaction (qRT-PCR) and immunofluorescence (IF) with primers and antibodies specific for meiotic genes. The meiotic genes we have

analyzed are presented in Table 3.2 which also reports their function, specificity for meiosis, and status in somatic tumor cell lines as described in the literature. These genes were chosen for their role in chromosome pairing and recombination, all events that favor genetic redistribution and, in our studies, might play a role during depolyploidization of MC cells.

<div align="center">mRNA Measurements</div>

To determine the up-regulation of the meiosis specific genes, SuperArray experiments were performed using HeLa S3, MDA-MB435, and FaDu (human head and neck cancer) cells. For each cell line, cells were irradiated with 5Gy of gamma-rays and samples were collected every 24 hours for 12-20 days in time-course experiments. The genes with which the SuperArray was constructed are reported in Table 3.3 and their mRNA expression in Figures 3.8-3.10. Cyclin B1 (CCNB1) was also included as the up-regulation of the protein had been documented as a hallmark of radiation-induced MC [Ianzini and Mackey, 1997]. As discussed for mitosis, cyclin B1 is required for the G2/M transition, but it also plays a role in meiosis, when in its phosphorylated state cyclin B1 promotes oocyte maturation during meiosis I [Westendorf *et al.*, 1989]. The results from the SuperArray were generated using the $2^{\Delta\Delta Ct}$ method of analysis for RT-PCR, a semi-quantitative measurement. In HeLa S3 (Figure 3.8) nearly all of the genes tested are up-regulated at both day 4 and day 8 post-irradiation. In MDA-MB435 cells (Figure 3.9) most of the genes are up-regulated at day 2 and day 4. In FaDu cells (Figure 3.10) all genes are up-regulated on one or more days with the exception of SYCP3. The Rad51AP2 gene was detected in all of these cells lines however the efficiency of these primers was not within the range acceptable for the $2^{\Delta\Delta Ct}$ method of analysis, and thus it was not reported for the superarray data.

Quantitative measurements of mRNA expression for these meiotic genes were assessed using qRT-PCR techniques. Quantitative RT-PCR was performed on HeLa S3,

MDA-MB435, and FaDu cells collected every 24 hours from control and irradiated populations in time course experiments. Analyses of expression of these genes reveals that Rec8 (Figure 3.11) is significantly up-regulated in irradiated HeLa S3 cells at days 4, 8, 16, 18, and 20, with a peak increase of 7-fold at day 4. SYCP3 (Figure 3.12) increases on days 4-8, 11, and 18-20 in irradiated HeLa S3 cells, with the greatest increases of 5-7 fold at days 5, 6, and 8. Other up-regulated genes in irradiated HeLa cells (data not shown) were Rad51AP2 and Cyclin B1 that presented significant increases from 2-4 days post-irradiation. Measurements of mRNA for Rad51AP2 were also conducted in FaDu cells, Figure 3.13 shows significant increases in the gene product at days 0, 2, 6, and 8. MDA-MB435 cells irradiated with 5Gy gamma rays were tested for DMC1 (Figure 3.14) and significant expression was found at days 0, 2, and 5 post-irradiation, with a maximum, 3-fold increase, at day 2. SPO11 (Figure 3.15) mRNA is up-regulated 2 to 3-fold in 5Gy irradiated MDA-MB435 cells at days 4, 5, and 6. Collectively these data support the hypothesis that meiotic genes are up-regulated in irradiated cancer cells with the most significant increases found at the time of increased multipolar divisions in MDA-MB435 and HeLa cells as described in the experiments carried out using LSDCAS (Figures 3.3B and 3.4B).

## Protein Measurements

Parallel studies with IF were conducted to verify that the mRNA is translated into functional protein and that the proteins are localized in the nucleus to indicate meiotic activity. IF staining for DMC1 in irradiated HeLa cells is presented in Figure 3.16 and shows protein aggregates in the nuclei, as was observed in actively dividing testes cells, suggesting that DMC1 is functional and is correctly localized for meiotic activity. HeLa cells in Figure 3.17A shows the presence of SYCP3 structures similar to those present in actively dividing testes cells (Figure 3.17B). Note, that although SYCP3 is present at low levels in the control cells (Figure 3.17C), the staining is diffuse in the cytoplasm and SC

structures are absent in the nuclei. CyclinB1 staining (Figures 3.17C-E) confirms that these cells are mitotically active.

## Conclusions

Through the combination of live cell imaging and traditional laboratory techniques we have shown that the timing of multipolar divisions is concurrent with the following measurements from MC cells: reduction of DNA content, observation of morphological features unique to meiosis, and up-regulation of meiosis specific genes. Additionally, we determined that MC cells can successfully produce mononucleated cell progeny through multipolar divisions and some of those progeny are viable and mitotically active. These observations reinforce the hypothesis that cells may initiate pathways to reduce their ploidy and recover from potentially lethal damage induced by radiation. The implications for meiosis as a pathway to reduce DNA content following radiation-induced MC warrants further investigation to determine if recombination events are occurring and to test the resistance of these cells to additional radiation treatments. We have already isolated and expanded one such clone from MDA-MB435 cells (data not shown) and are proceeding with experiments to determine the genetic profile of these cells as compared to the original cell line and also to evaluate their resistance to further radiation treatment.
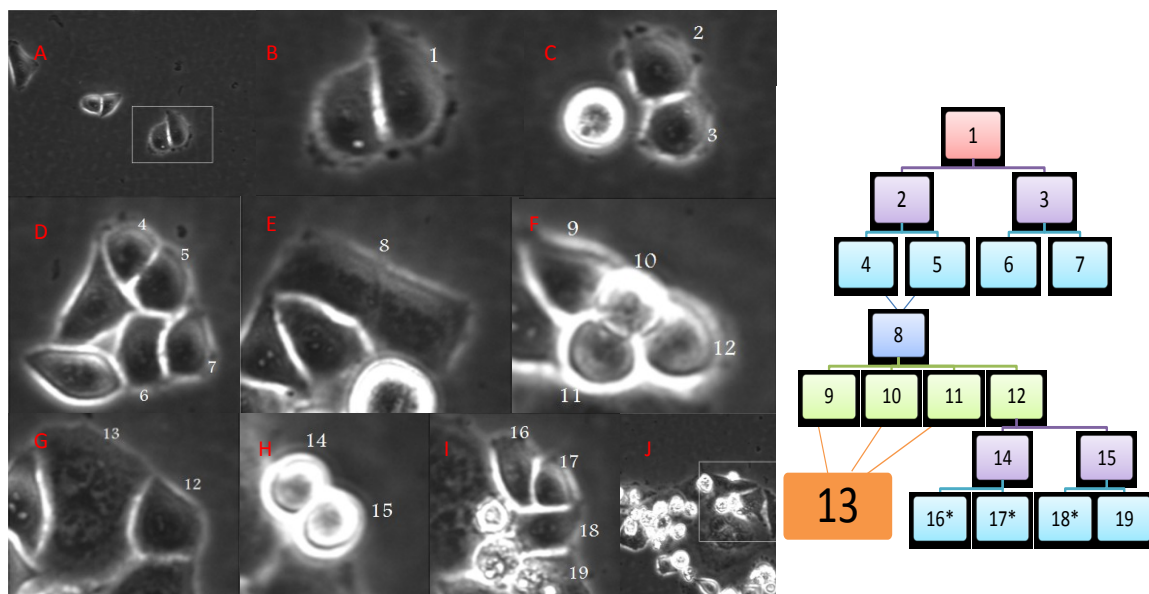
Figure 3.1: HeLaS3 cells irradiated with 5Gy gamma rays were imaged for three weeks, beginning 27 hours post-irradiation. The images on the left are still shots from a time-lapse movie created with LSDCAS and the graph on the right shows the connectivity of the cells labeled in the images. **A** - An image of the entire field of view. The boxed cells were enlarged in the following images (B-I) to show the series of events surrounding a possible reductive division. **B** - 27hrs post-irradiation. The cell labeled *1* is the parent cell. It is mononucleated and of average size for HeLaClone3 cell culture. **C** - 32hrs post-irradiation. Cell *1* divided normally to produce two mononucleated daughter cells shown here during interphase, labeled *2* and *3*. **D** - 53 hours post-irradiation. Cell *2* successfully completed a normal division to produce cells *4* and *5*. Cell *3* successfully completed a normal division to produce cells *6* and *7*. **E** - 72 hours post-irradiation. Cells *4* and *5* fuse to form the bi-nucleated cell labeled *8*. **F** - 75 hours post-irradiation. Cell *8* attempts a multipolar division to form cells *9*, *10*, *11*, and *12*. **G** - 82 hours post-irradiation. Cells *9*, *10*, and *11* fail to segregate and immediately fuse to form one large multinucleated cell (*13*). Cell *12* remains independent, is mononucleated, and of normal size. **H** - 101 hours post-irradiation. Cell *12* has just completed a normal division to produce mononucleated daughter cells *14* and *15*. The image shows that division proceeded normally and was not a failed multipolar attempt. **I** - 137 hours post-irradiation. Cell *14* has completed a successful division to produce cells *16* and *17*. Cell *15* has completed a successful division to produce cells *18* and *19*. **J** - 11 days and 2 hours post-irradiation. An image of the entire field of view shows cells *16*, *17*, and *18* have stayed within the field of view and are still alive*.

## A - Yield of Normal Division Events in MDA-MB435 Cells After Gamma Irradiation



## B - Yield of Multipolar Division Events in MDA-MB435 Cells After Gamma Irradiation
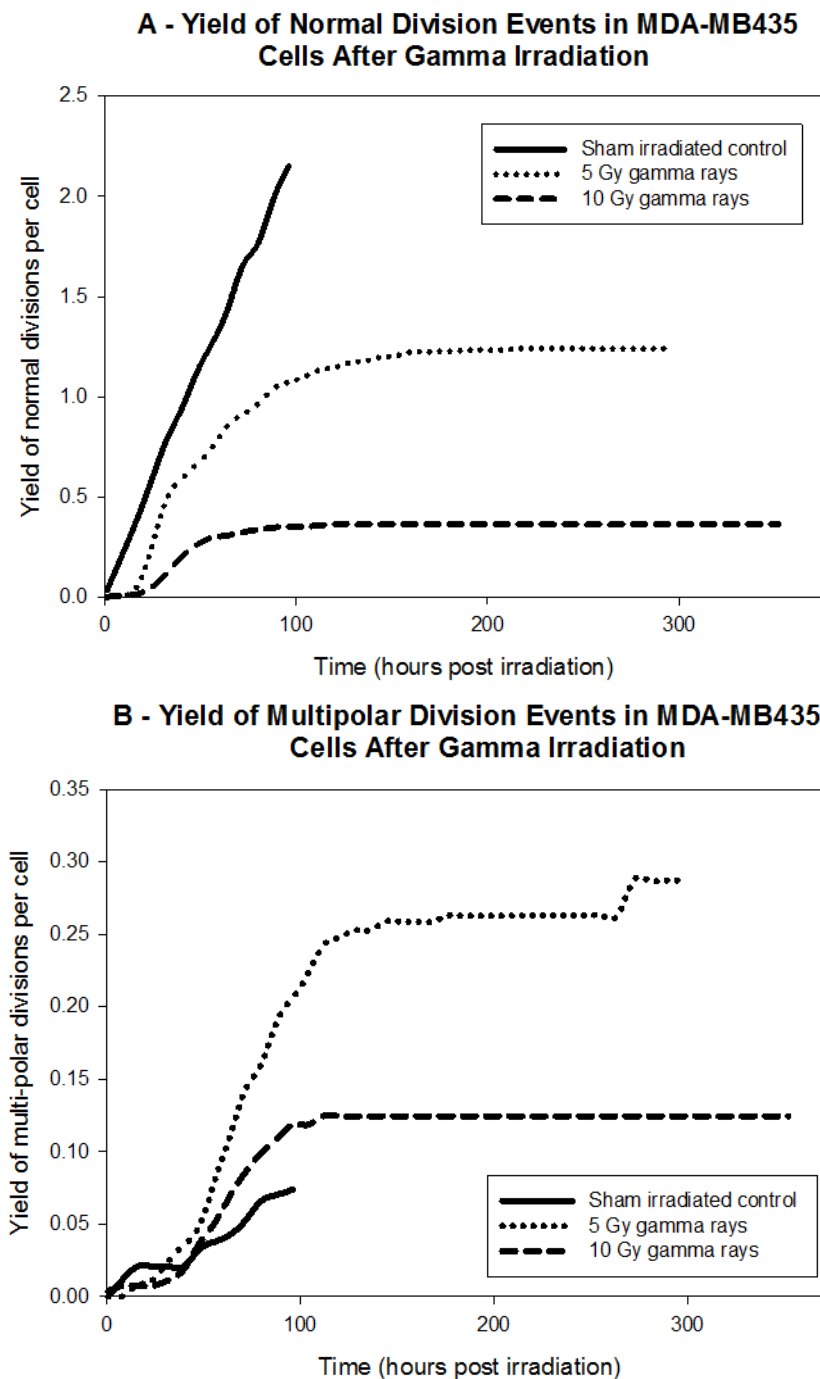


Figure 3.2: Yield of cellular events in MDA-MB435 cells undergoing radiation-enhanced MC. Following treatment, image acquisition proceeded for 14 days, followed by manual event detection and yield analysis for [A] normal division, [B] multipolar division, [C] cell fusion, and [D] cell death.

Figure 3.2 continued



**C - Yield of Fusion Events in MDA-MB435 Cells After Gamma Irradiation**



**D - Yield of Death Events in MDA-MB435 Cells After Gamma Irradiation**
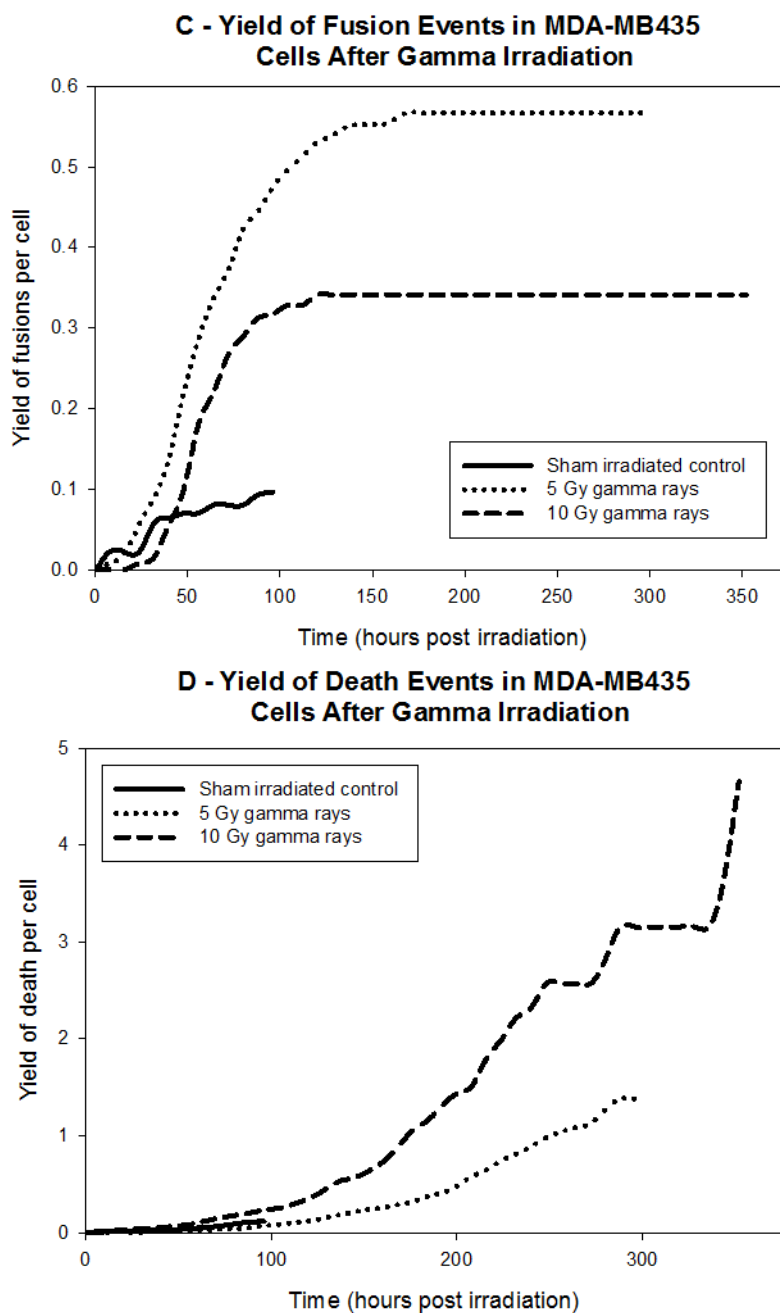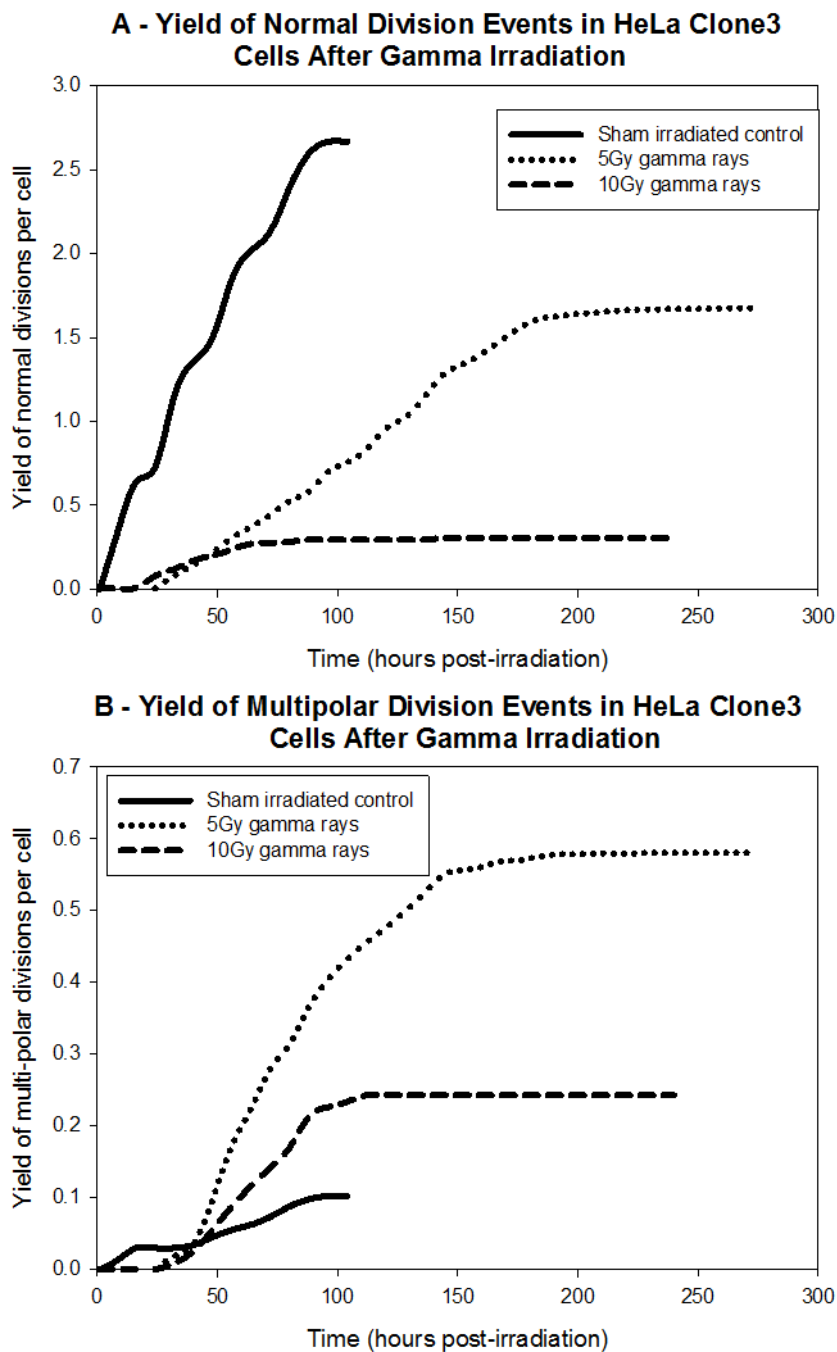
Figure 3.3: Yield of cellular events in HeLa Clone 3 cells undergoing radiation-enhanced MC. Following treatment, image acquisition proceeded for 12 days, followed by manual event detection and yield analysis for [A] normal division, [B] multipolar division, [C] cell fusion, and [D] cell death.

Figure 3.3 continued



**C - Yield of Fusion Events in HeLa Clone3 Cells After Gamma Irradiation**

**D - Yield of Death Events in HeLa Clone3 Cells After Gamma Irradiation**
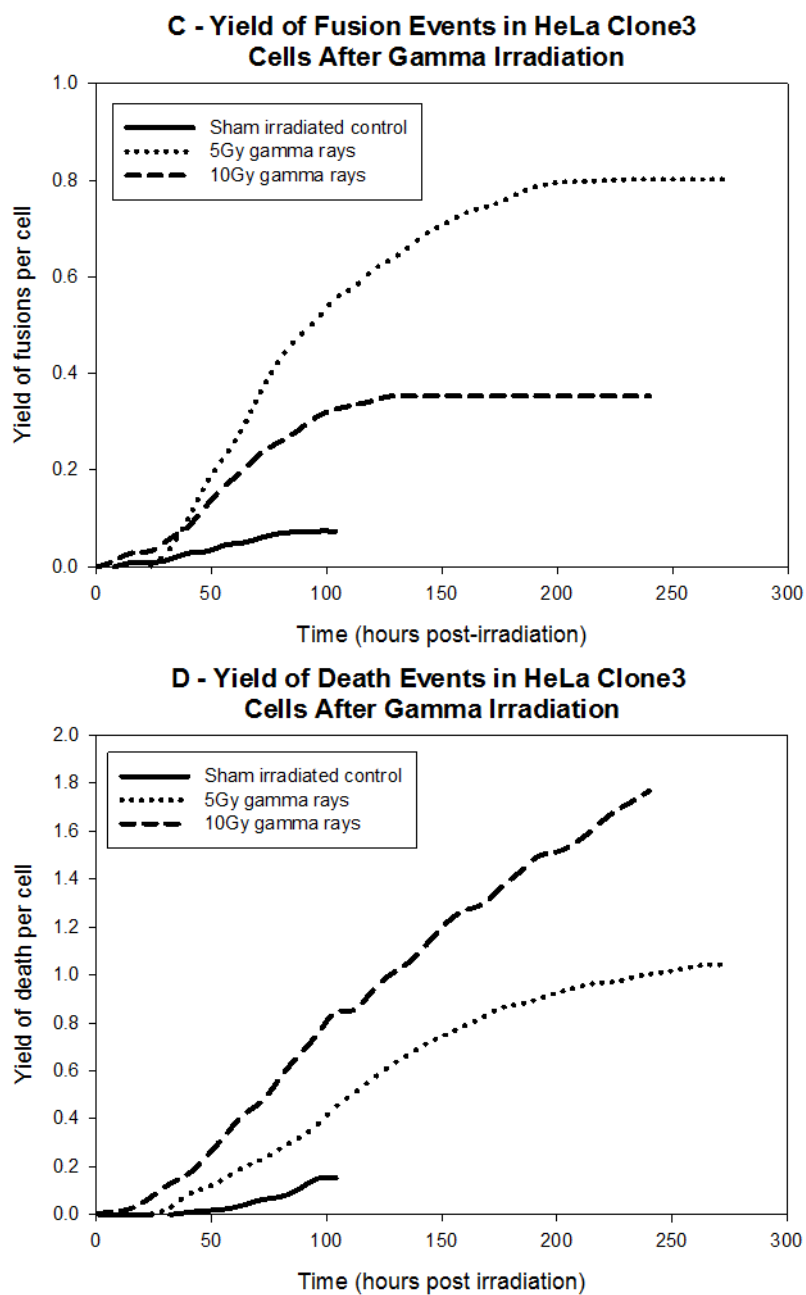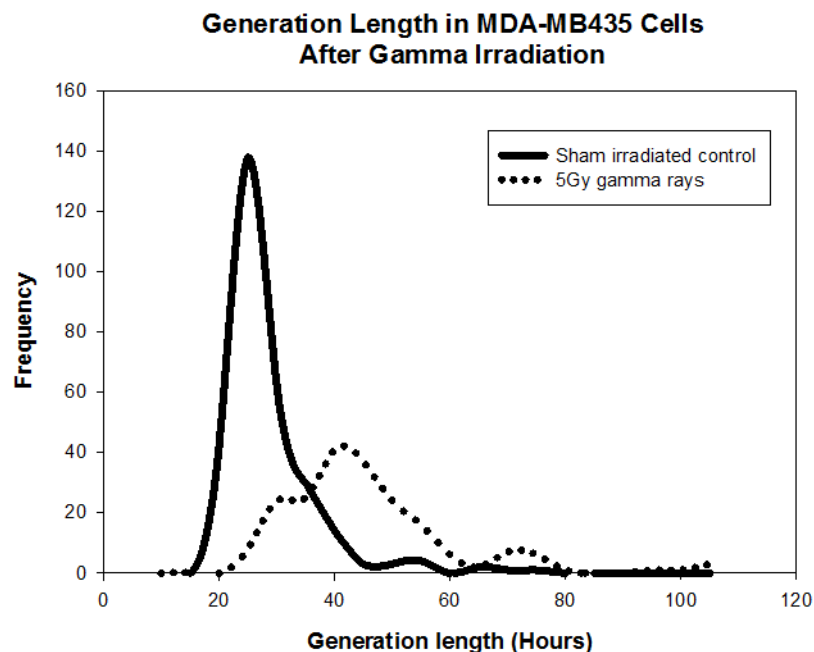
Figure 3.4: Generation analysis using the subgraph isomorphism algorithm in MDA-MB435 cells. The query used defines a graph that begins with a normal division (ND) producing a mononucleated daughter (FO) which rounds up (RU) and divides normally again (ND). The generation length was calculated as the time between normal division events in the returned subgraphs.

| | Generation Length (h) | | Mitosis Length (h) | |
|---|---|---|---|---|
| | Control | Treated | Control | Treated |
| Mean | 26 | 43.7 | 0.9 | 1.9 |
| Median | 23.8 | 40.4 | 0.7 | 1.3 |
| Std Dev | 7.9 | 17.9 | 1.1 | 2.5 |
| Std Error | 0.45 | 1.26 | 0.05 | 0.12 |
| 25% | 21.5 | 33.9 | 0.5 | 0.9 |
| 75% | 27.9 | 46.9 | 0.9 | 1.7 |
| n | 300 | 202 | 376 | 428 |

Table 3.1: **Statistical analysis of generation length and time to complete mitosis in MDA-MB435 cells.**

Statistical comparison shows significant increases in both generation length and mitosis length for 5Gy gamma irradiated MDA-MB435 cells as compared to sham irradiated controls (Mann-Whitney rank test p=<0.001)
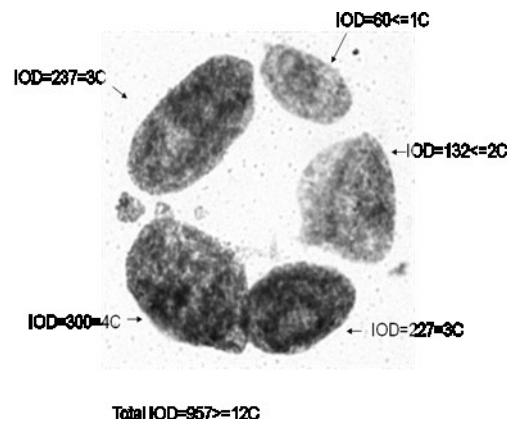
Figure 3.5: DNA measurements HeLa Clone3 cells 6 days after 10Gy-irradiation. This image shows an example of the uneven distribution of DNA into nuclear fragments. The cells were prepared with a Toloudine Blue stain after complete digestion of the cytoplasm with HCl. The optical densities of control cells on the same slide were measured to obtain the approximate optical density associated with 2C genomes.
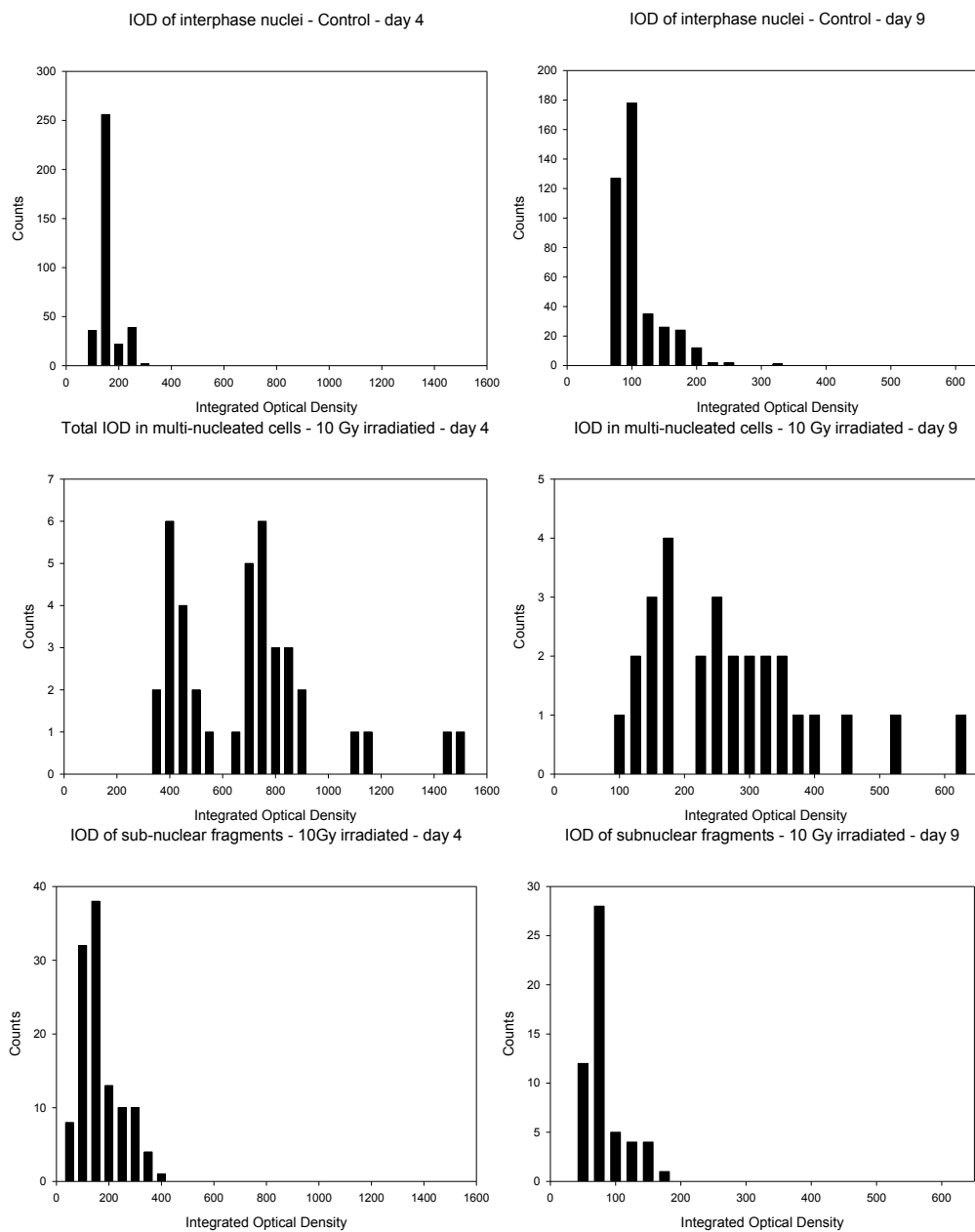
Figure 3.6: DNA measurements in irradiated HeLa cells after 10Gy gamma irradiation. Total DNA content as well at sub-nuclei DNA content were measured at day 4 and day 9 post-irradiation in MC cells using optical densitometry. Distributions of DNA content are shown above in control interphase cells and 10Gy irradiated interphase cells.

| Parameters | Non-treated | 10Gy-d.4 | 10Gy-d.9 |
|------------|-------------|----------|----------|
| OD std dev | 0.2 | 0.29 | 0.1 |
| Area std dev | 137 | 387 | 195 |
| IOD std dev | 31.7 | 77.7 | 39.6 |

Table 3.2: **DNA image cytometry measurements reveal reduction of DNA content days after irradiation.**

Parameters obtained from collective DNA image cytometry on control and 10Gy gamma irradiated HeLaS3 cells. Standard deviations of optical density, integrated optical density, and area give insight to the uniformity of cell texture, heterogeneity of DNA, and shape in the overall population.
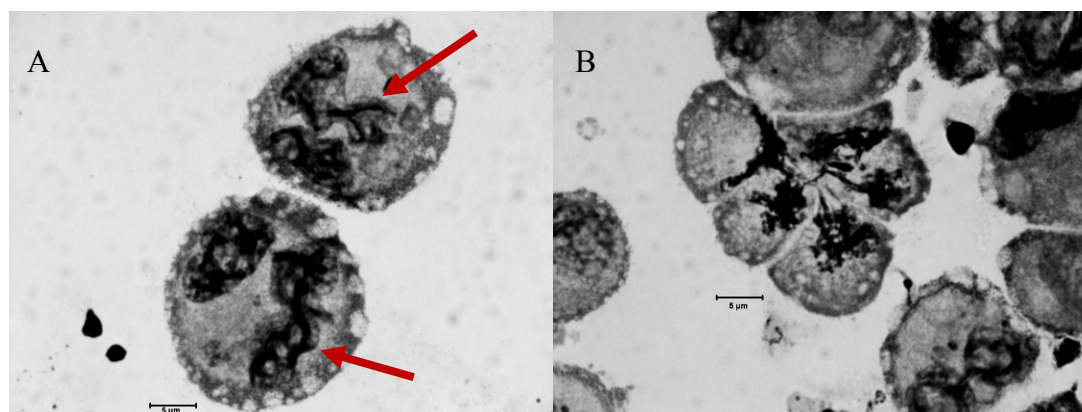


Figure 3.7: HeLaS3 cells 7 days after irradiation with 10Gy gamma rays. [A] Arrows indicate what may possibly be synaptonemal complexes in the condensed chromatin. [B] A multipolar division depicting thin DNA strands between sub-nuclei. The cells were prepared with a Toloudine Blue stain after gentle digestion of the cytoplasm with HCl.

| Gene | Function | Function is specific to meiosis | Expressed in somatic tumor cells |
|---|---|---|---|
| SPO-11 | A transesterase capable of inserting DNA double stand breaks in homologous chromosomes for strand exchange | X | X |
| Rec8 | Cohesin complex protein that interacts with SMC1 and SMC3 to hold sister chromatids together during meiosis | X | |
| Rad51 | Catalyzes homologous DNA pairing and strand exchange between sister chromatids (recombination) | | X |
| Rad51-AP | Associates with Rad51 during meiosis to accomplish intrahomologous recombination | X | |
| DMC1 | Catalyzes homologous DNA strand exchange between homologous chromosomes (recombination) | X | X |
| STAG3 | Cohesin complex protein that interacts with SMC1 and SMC3 to hold sister chromatids together during meiosis | X | X |
| MOS | Aides in the maturation of oocytes by causing cell cycle arrest in M-phase, upstream activator of MAPK pathway | X (oocytes) | X |
| SYCP1 | Forms the central elements of the synaptonemal complex, completes synapsis of the homologous chromosomes | X | X |
| SYCP2 | Stabilizes cohesin complex along the chromosomal axis and forms the lateral element of the synaptonemal complex | X | X |
| SYCP3 | Stabilizes cohesin complex along the chromosomal axis and forms the lateral element of the synaptonemal complex | X | X |

Table 3.3: **Meiotic genes involved in synaptonemal complex formation and recombination events.**

Meiotic genes of interest, their functions, specificity to meiosis and expression status in tumor cell lines. [Romanienko 1999, Raderschall 2002, Harad 2001, Erenpresia 2006, Propst and VandeWalde 1985. Gorgoulis 2001, UCSC Human Gene Sorter 2008]
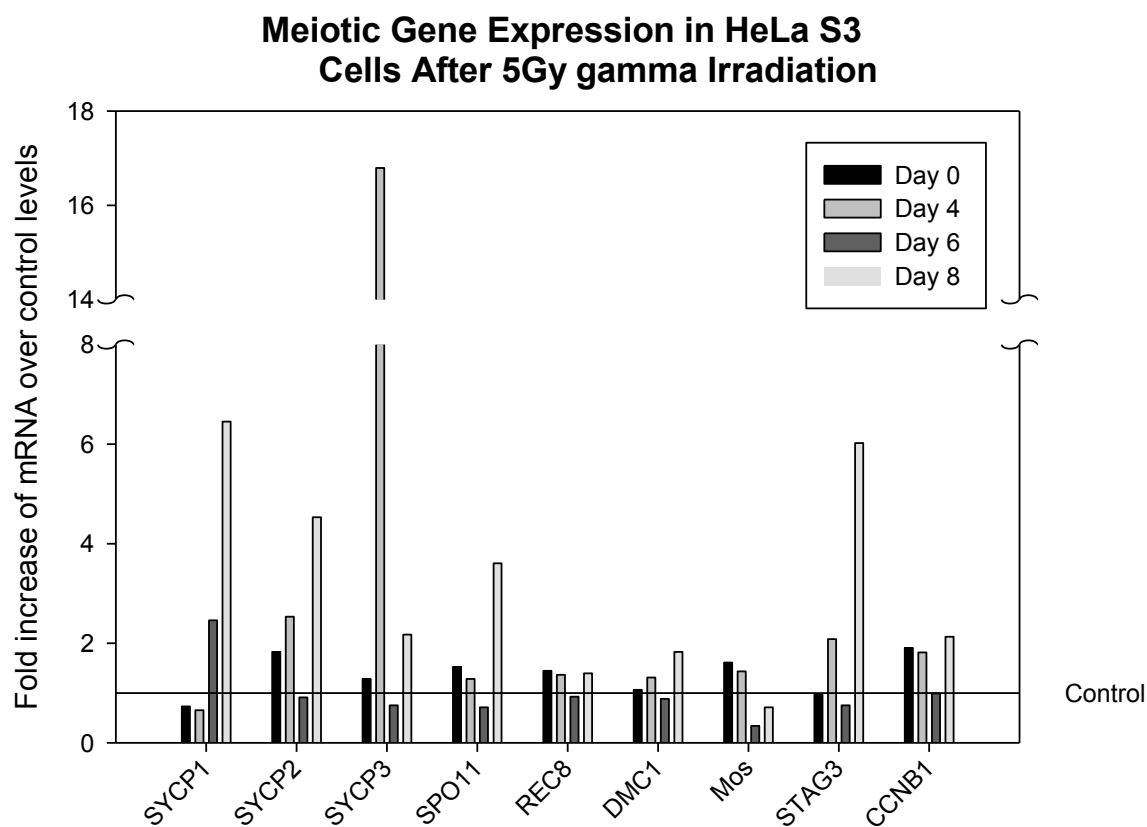
Figure 3.8: Meiotic gene expression in HeLa S3 cells after 5Gy gamma irradiation. Data are presented from days 0, 4, 6, and 8 as fold-increase of mRNA after normalization with control samples. RT-PCR reactions were run in duplicate using a *SuperArray* designed to detect a variety of meiotic genes and were normalized to RPLPO for loading error. Above is a representative of the two experiments.
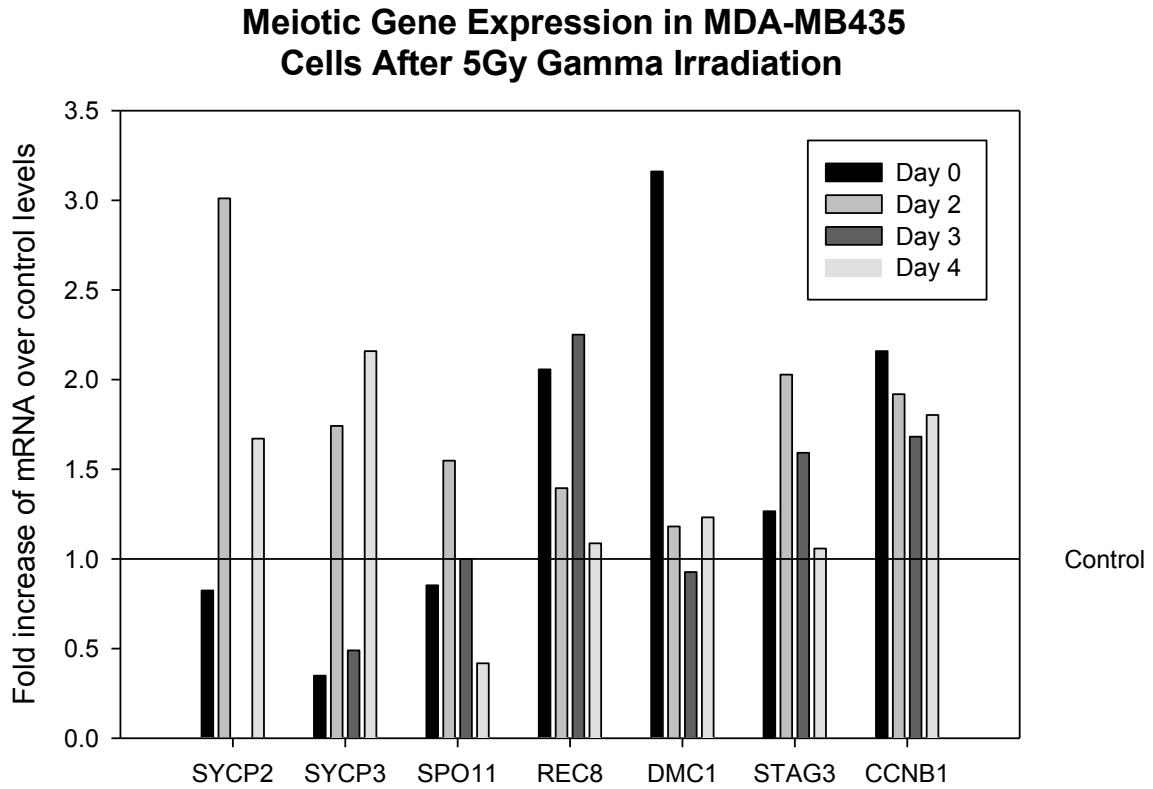
Figure 3.9: Meiotic gene expression in MDA-MB435 cells after 5Gy gamma irradiation. Data are presented from days 0, 2, 3, and 4 as fold-increase of mRNA after normalization with control samples. RT-PCR reactions were run in duplicate using a *SuperArray* designed to detect a variety of meiotic genes and were normalized to RPLPO for loading error. Above is a representative of the two experiments.
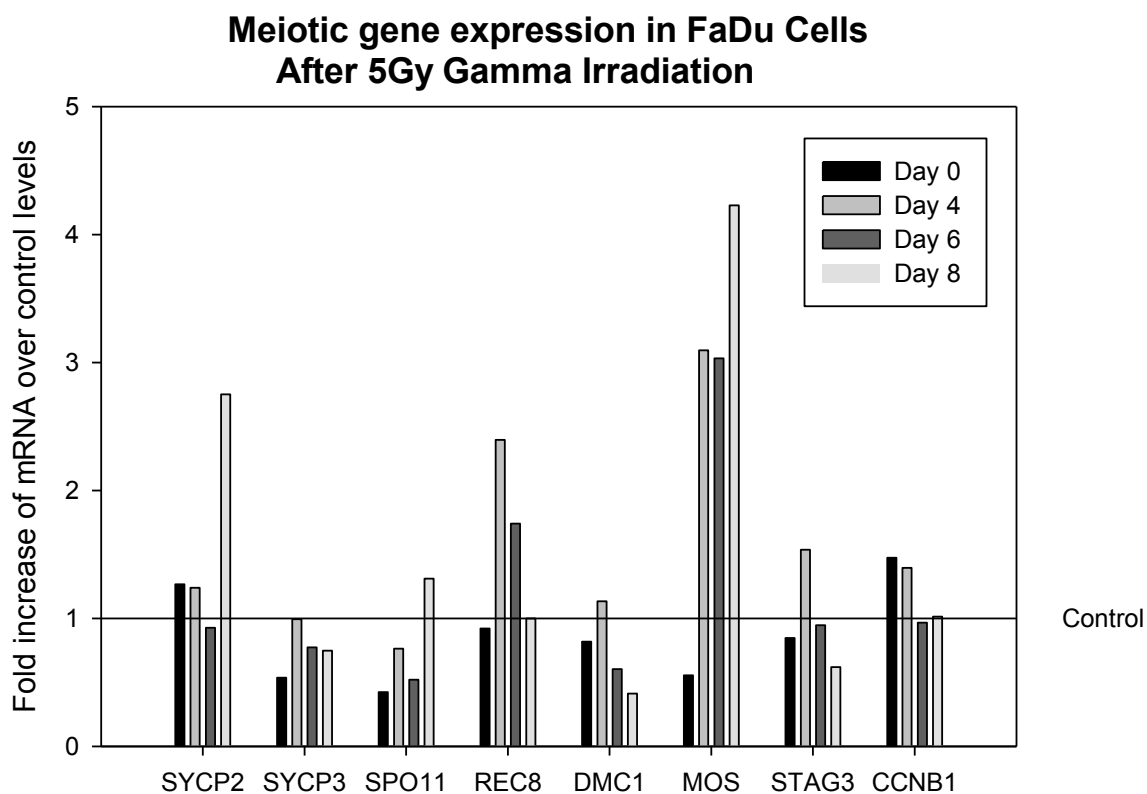
Figure 3.10: Meiotic gene expression in FaDu cells after 5Gy gamma irradiation. Data are presented from days 0, 4, 6, and 8 as fold-increase of mRNA after normalization with control samples. RT-PCR reactions were run in duplicate using a *SuperArray* designed to detect a variety of meiotic genes and were normalized to RPLPO for loading error. Above is a representative of the two experiments.

# Rec8 Expression in HeLa S3 Cells After Gamma Irradiation
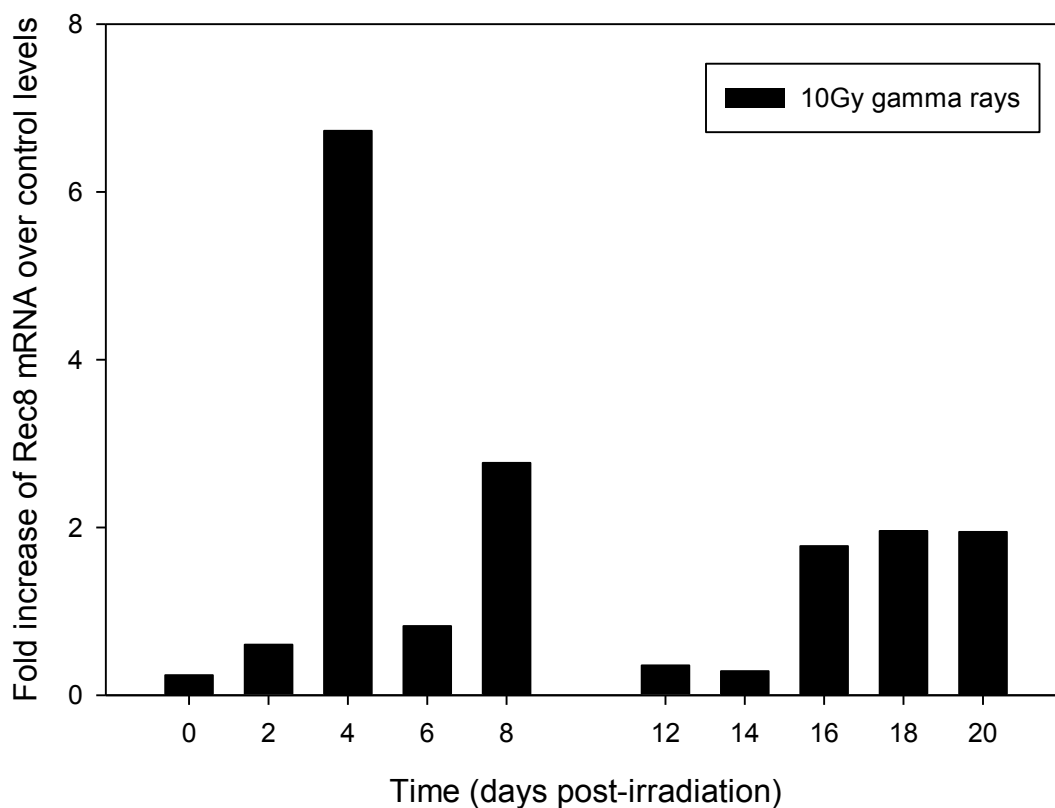


Figure 3.11:  Rec8 expression in HeLaS3 cells after gamma irradiation. HeLaS3 cells
were irradiated with 10Gy gamma irradiation and samples collected at 24 hour
intervals for 20 days.  Data are presented as fold-increase after normalization
with control samples. qRT-PCR reactions were run in triplicate using primer
and probes designed by ABI to detect Rec8 mRNA and were normalized to
RPLPO for loading error.  Standard curves were run using human testes
cDNA.

# SYCP3 Expression in HeLa S3 Cells After Gamma Irradiation
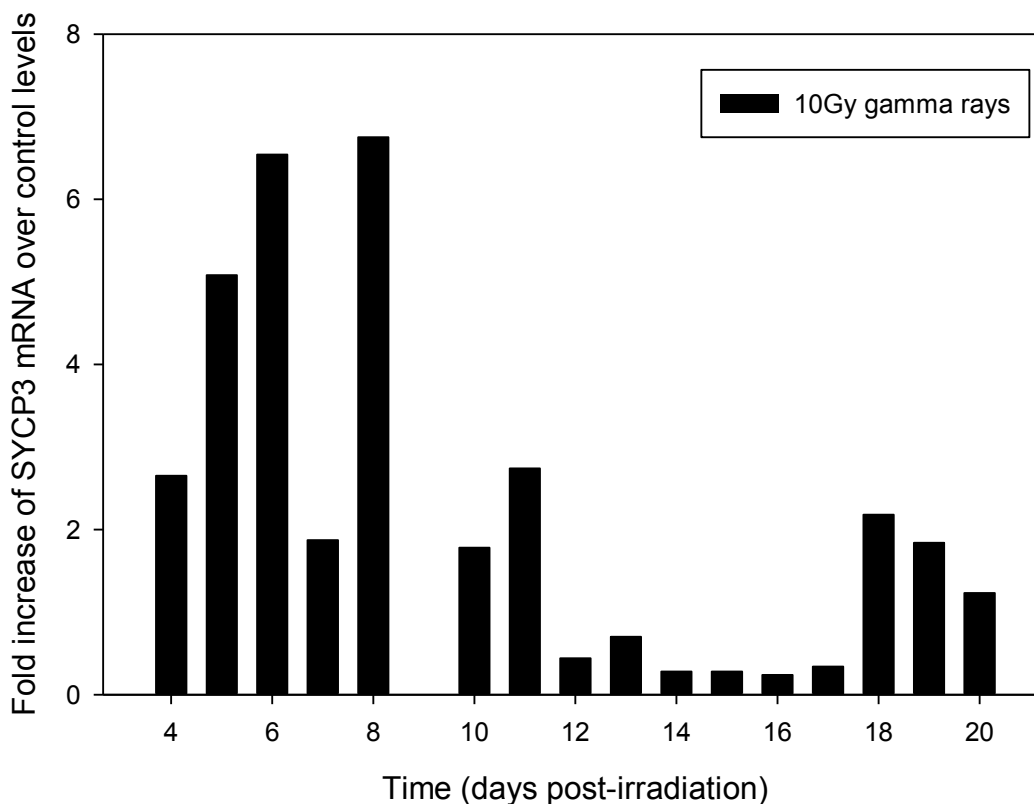


Figure 3.12: SYCP3 expression in HeLaS3 cells after gamma irradiation.  HeLaS3 cells were irradiated with 10Gy gamma irradiation and samples collected at 24 hour intervals for 20 days.  Data are presented as fold-increase after normalization with control samples. qRT-PCR reactions were run in triplicate using primer and probes designed by ABI to detect SYCP3 mRNA and were normalized to RPLPO for loading error.  Standard curves were run using human testes cDNA.

## Rad51AP2 Expression in FaDu Cells After Gamma Irradiation
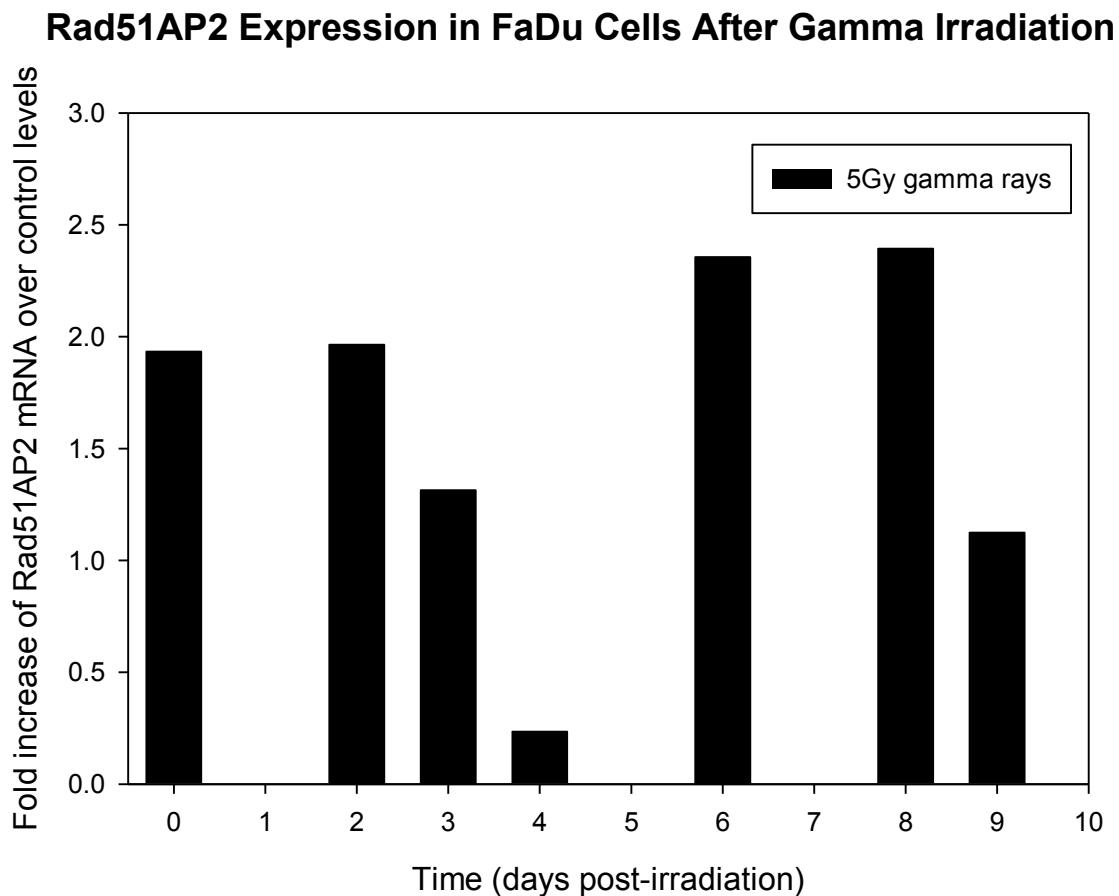


Figure 3.13: Rad51AP2 expression in FaDu cells after gamma irradiation. FaDu cells were irradiated with 5Gy gamma irradiation and samples collected at 24 hour intervals for 12 days. Data are presented as fold-increase after normalization with control samples. qRT-PCR reactions were run in triplicate using primer and probes designed by ABI to detect Rad51AP2 mRNA and were normalized to RPLPO for loading error. Standard curves were run using human testes cDNA.

# DMC1 Expression in MDA-MB435 Cells After Gamma Irradiation
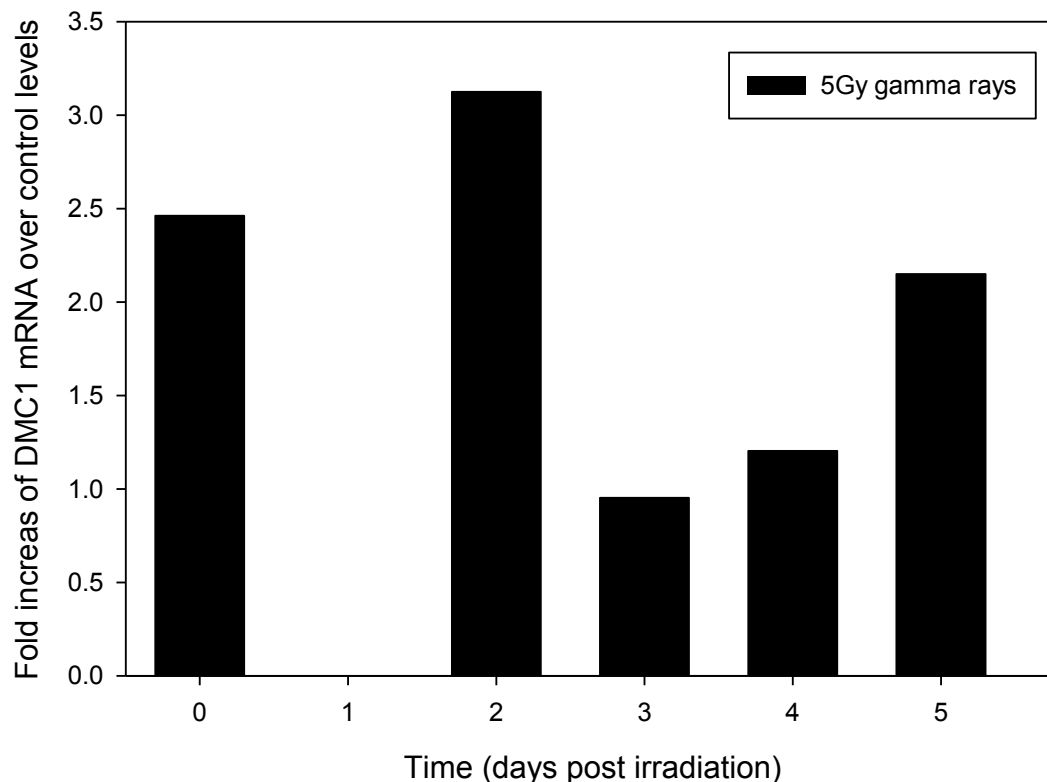


Figure 3.14: DMC1 expression in MDA-MB435 cells after gamma irradiation. MDA-MB435 cells were irradiated with 5Gy gamma irradiation and samples collected at 24 hour intervals for 12 days. Data are presented as fold-increase after normalization with control samples. qRT-PCR reactions were run in triplicate using primer and probes designed by ABI to detect DMC1 mRNA and were normalized to RPLPO for loading error. Standard curves were run using human testes cDNA.

## SPO11 Expression in MDA-MB435 Cells After Gamma Irradiation
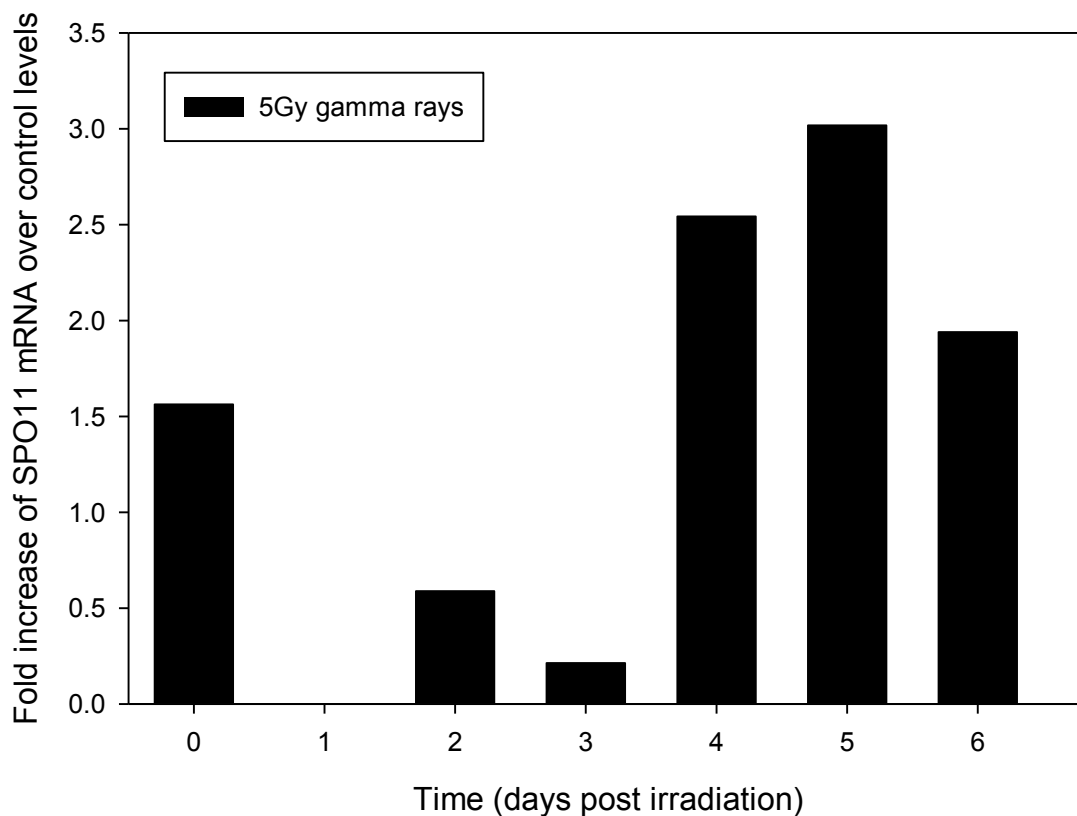


Figure 3.15: SPO11 expression in MDA-MB435 cells after gamma irradiation. MDA-MB435 cells were irradiated with 5Gy gamma irradiation and samples collected at 24 hour intervals for 12 days.  Data are presented as fold-increase after normalization with control samples. qRT-PCR reactions were run in triplicate using primer and probes designed by ABI to detect SPO11 mRNA and were normalized to RPLPO for loading error.  Standard curves were run using human testes cDNA.
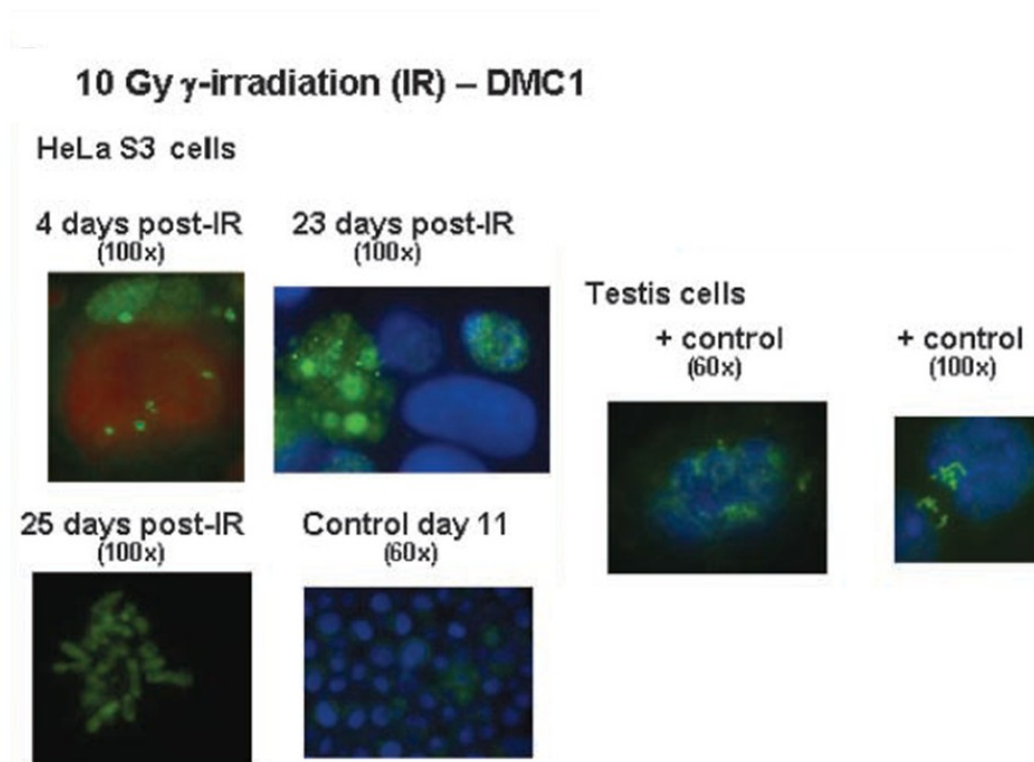
Figure 3.16: DMC1 protein expression in HeLa S3 cells following 10Gy gamma
irradiation. Focal staining of DMC1 (green) is visible at various times post-
irradiation. Condensed chromosomes are also visible at 25 days post-
irradiation. Positive controls: untreated mouse testis cells. IF was performed
using primary antibody: DMC1 (1:100 dilution; Abcam); secondary antibody
goat anti-mouse FITC IgG (whole molecule, 1:100 dilution; Sigma);
counterstaining 4,6-diamidino-2-phenylindole (DAPI-red or blue).

**HeLa S3 cells   5 Gy γ-Radiation (IR) – SYCP3 and Cyclin B1**

**A – 6 days post-IR**

**B - Testes cells   + control**

**C – Control 6 days (40X)**

**D – 5 days post-IR (20X)**
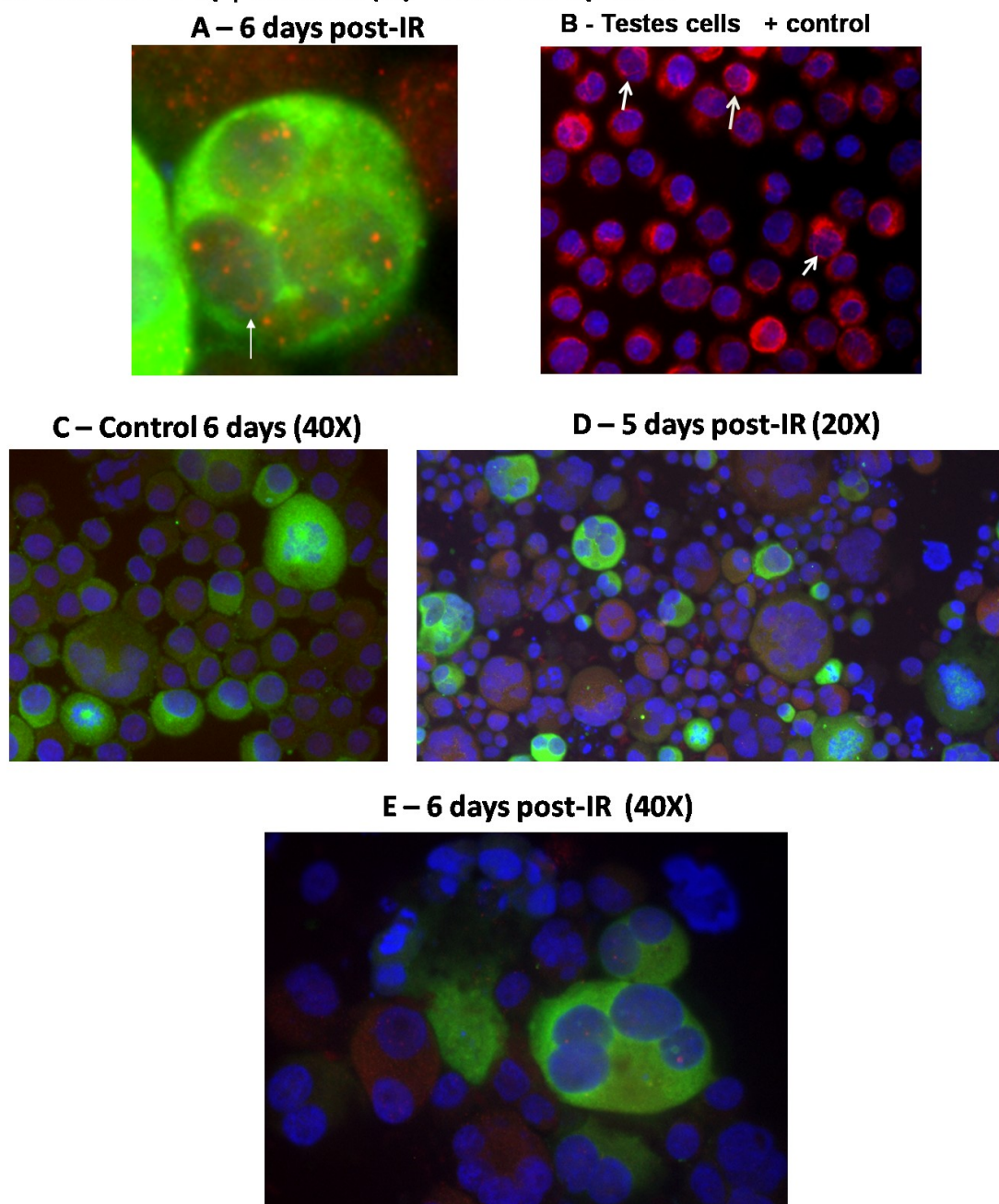
**E – 6 days post-IR  (40X)**



Figure 3.17: SYCP3 and cyclin B1 protein expression in HeLa S3 cells following 5Gy gamma irradiation.  [A] 6 days post-IR (40X objective + enlarged 100% to accentuate SC)  [B] Mouse testes cells positive (+) control for SC structure - (40X objective + enlarged 100% to accentuate SC)  [C]  HeLa S3 cells control day 6 (40X objective) [D] 5 days post-IR (20X objective) [E] 6 days post-IR (40X objective).  IF was performed with anti-bodies to CyclinB1 (green – Millipore 1:25/Invitrogen 1:500) and SYCP3 (red – Abcam 1:50/Invitrogen 1:500).   DAPI was used to counter stain nuclei (blue – Vector Labs).

CHAPTER 4

BLUE FLUORESCENCE EXCITATION LIGHT: TOXICITY ISSUES

FOR LIVE CELL FLUORESCENCE MEASUREMENTS

LSDCAS has been upgraded from its original design to include epifluorescence capabilities; this included the addition of a mercury arc lamp light source, a UV filter in the light path, and filter wheels for emission, excitation, and neutral density filters. Control of the light source and filter wheel were built into the existing acquisition program so that during an experiment the microscope can switch between grey scale and fluorescence image acquisition. The existing protocols and imaging systems for live cell fluorescence measurement are primarily optimized for short-term fluorescence exposure. Thus, development of biological protocols for fluorescent dye loading was required to make live cell fluorescence measurements over long periods of time. Interaction of the probe with the loading buffer, osmolarity effects from the buffer, and efflux of the dyes from the cells, all can contribute to poor image quality. Beyond accurate fluorescence measurement, long term experiments may be hindered by toxicity from intense excitation light either in large doses or small doses over extended periods.

The toxic effect of fluorescence excitation light on cell culture has been known since the late 1970's, and has been attributed to the production of intracellular peroxides. Cells exposed to UV or blue light have been shown to produce $H_2O_2$ in peroxisomes and mitochondria [Wang and Nixon 1978, Bradley and Sharkey 1977, Hockberger *et al.* 1999]. Intracellular $H_2O_2$ is metabolized by the cell to produce hydroxyl radicals which can interact with and damage the cell's macromolecules [Kellogg and Fridovich 1975, reviewed in Valko *et al.* 2004]. With the introduction of UV and neutral density filters for use in fluorescence microscopy it has been taken for granted that the damaging wavelengths are removed from the excitation light delivered to cells. However, there has

been no conclusive study to determine if long term exposure to even the filtered light has phototoxic effects.

### Effects of Graded Neutral Density Filters on Excitation

### Light-Induced Toxicity

The application of LSDCAS and the event analysis programs have been instrumental to determine the toxic effects of fluorescence excitation light on growing cell populations. We examined the effect of varying the overall excitation light intensity by using the lowest and highest neutral density filters available in a standard filter set (ND1 and ND6). Cells were exposed to 1.5 seconds of blue excitation light every 7 minutes for 3 days, varying only the neutral density filter used between samples. After image acquisition was complete, manual event analysis for cell division and cell death parameters was used in conjunction with the yield analysis. The results reported in Figure 4.1 show that the lowest neutral density filter provides no protection from the intense excitation light, while the highest neutral density filter reduced cell death remarkably. Every cell imaged with the least filtered excitation light either lysed or became rounded and detached from the flask surface. No division parameters are reported because the blue fluorescence excitation light induced cell death so quickly the cells could not complete division when the lowest neutral density filter was used, this effect was immediate and occurred in every cell that was imaged.

### Effects of Bulb Age on Excitation Light-Induced Toxicity

Early light toxicity data showed inconsistent results for cell growth while varying interleave between the grey scale and fluorescent images. However, a trend was observed where the cell culture proliferated less, immediately after a new mercury bulb was installed. According to manufacturer's specifications, the mercury bulb is expected to give consistent illumination for up to 200 hours. To determine if the biological effect was a result of bulb age, a series of images were captured over the life of the mercury

bulb (3 experiments lasting 3 days each). Blue fluorescence excitation light was delivered to the human head and neck cancer cell line, FaDu. The cells were not labeled with a probe and do not express any fluorescent molecule such as green fluorescent protein (GFP), therefore any damage or biological effects should be due solely to excitation light toxicity. The exposure time for each image remained constant in all experiments at 1.5 seconds/frame with an interframe time of 7 minutes, due to the results from the light intensity experiment discussed above we used only the highest neutral density filter for this and all following experiments. The results from this experiment are shown in Figure 4.2, in which normal division data was manually identified in the image sequences and the yield of normal divisions are plotted over the time course of the experiment. At the beginning of the bulb's life span the yield of normal divisions after three days are reduced by about 60%. As the bulb ages the cells are resuming the rate of normal divisions as in the control population showing a very clear graded biological effect as the light source decays. Death analysis (data not shown) did not show any significant variations from that in control cell populations when cells were exposed to blue fluorescence excitation light.

The experiment discussed above show that the FaDu cells are sensitive to the mercury lamp excitation light source, with highest toxic effects occurring when a freshly replaced bulb was used as compared to a bulb that was near the end of its useful lifetime. To determine if this sensitivity is carried across cell lines, the same experiment was performed using the MDA-MB435, human melanoma cell line. As with the FaDu, the exposure time (1.5 sec) and frequency (7 min) remained constant over a 72 hour period, with 3 consecutive experiments that spanned the usable life of a single bulb. The image sequences were analyzed for the yield of normal divisions (Figure 4.3A) and the data show approximately a 30% reduction in normal division events when a new bulb is used. Near the end of the bulb's usable life, normal divisions return to control levels. Death events were also detected and the yield analyses are reported in Figure 4.3B, showing a

3.5 times greater yield of death in cells illuminated with a new mercury bulb as compared to control populations. These results collectively show that MDA-MB435 cells are extremely sensitive to blue fluorescence excitation light both in the form of decreased cell division and increased cell death unless the excitation source has already experienced 6 days of use.

<div align="center">

Morphological Observations of Excitation Light-Induced

Toxicity

</div>

While we can measure the toxic effects of fluorescence excitation light on cells, examination of the morphology may also lead to insights about the mechanisms of the observed toxicity. Morphologically, both cell lines were less flattened to the cell surface during fluorescence excitation light exposure as compared to control cells. This effect was much more dramatic in the FaDu cells thus further morphological observations were hindered. Although defined intracellular morphology was not detectable in the FaDu cells, it was observed that while using the lowest neutral density filter (discussed above), these cells frequently rounded up and detached from the surface of the flask. Examining Figure 4.4 that shows light toxicity in MDA-MB435 cells, it is possible to notice that when the excitation source is newest (0-72 hours) the cells are larger than in the control population. Increase in cell size is an immediate sign of cellular stress, and this effect is attenuated when an older bulb is used (144-220 hours). Furthermore, the images contain bright pixel areas noticeable in cells experiencing fluorescence excitation light-induced toxicity (Figure 4.5 and highlighted with arrows in Figure 4.6). In normal situations of no toxicity we detect increased pixel intensity when cell membranes undergo what might be changes in fluidity at the time of cell division (see Chapter 2 and Figure 2.3). As a cell becomes more spherical the change in phase as light passes through the sample results in greater pixel intensity or bright white regions in the image. In the images discussed here we detect these bright areas beginning to form at 1 day of exposure and

they increase in number by 3 days of exposure. These features also move throughout the cell and could be part of the cell membrane.  Thus, it is possible that the observed brightness is related to changes in membrane fluidity and due to the toxic effects of fluorescence excitation light that may cause altered cell shape and/or attachment to the flask.

## Conclusions

Fluorescence excitation light induced-toxicity was measured in two different cancer cell lines using LSDCAS and the event analysis programs.  It was observed that both cell cultures are sensitive to blue fluorescence excitation light, however the effect is not always observed within the same parameters.  That is, for FaDu cells light toxicity does not induce cell death (when light is properly filtered for intensity) however a reduction in cell division events is apparent.  Conversely, for MDA-MB435, the primary effect of light toxicity is cell death, while reduction of normal divisions is only half that observed in the FaDu cells.  These observations illustrate the varied resistance to fluorescence excitation light toxicity between cell lines, a fact that needs to be taken into account when choosing a cell line for fluorescence live cell imaging experiments.  Further studies are required to elucidate the mechanism(s) of fluorescence excitation light toxicity and to develop technologies apt to prevent or circumvent these effects.
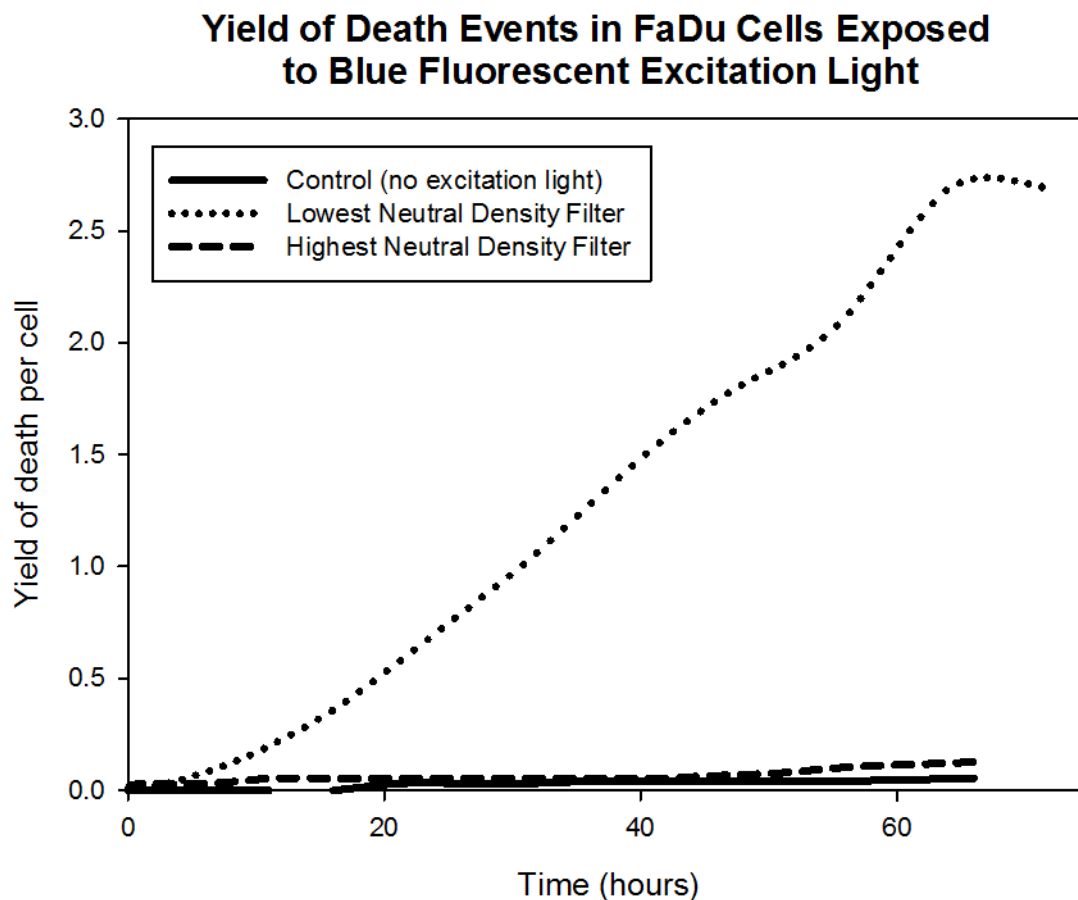
Figure 4.1: Yield of cell death in FaDu cells exposed to blue fluorescence excitation light using graded neutral density filters. Three consecutive experiments were conducted, a control that acquired only grey scale images and two that acquired both fluorescent and grey scale images. Each experiment lasted for 3 days and in the treated samples, the cells received blue light for 1.5 seconds every 7 minutes, and light intensity was filtered using either the hightest or lowest neutral density filter.

**Yield of Normal Division Events in FaDu Cells Exposed to Blue Fluorescent Excitation Light**
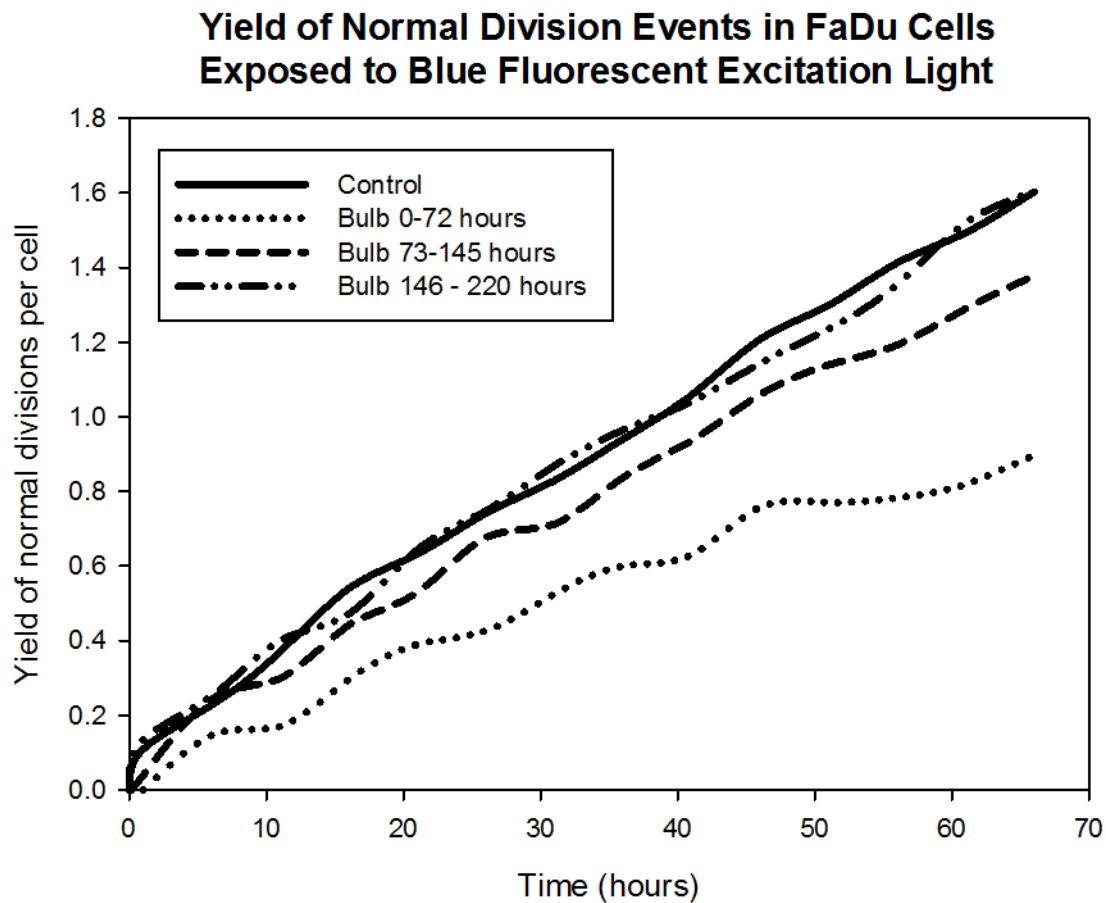
Figure 4.2: Yield of normal divisions in FaDu cells exposed to blue fluorescence excitation light. Four consecutive experiments were conducted, a control that acquired only grey scale images and three that acquired both fluorescent and grey scale images over the course of a mercury bulb's usable lifespan. Each experiment lasted for 3 days and in the treated samples, the cells received blue light for 1.5 seconds every 7 minutes.
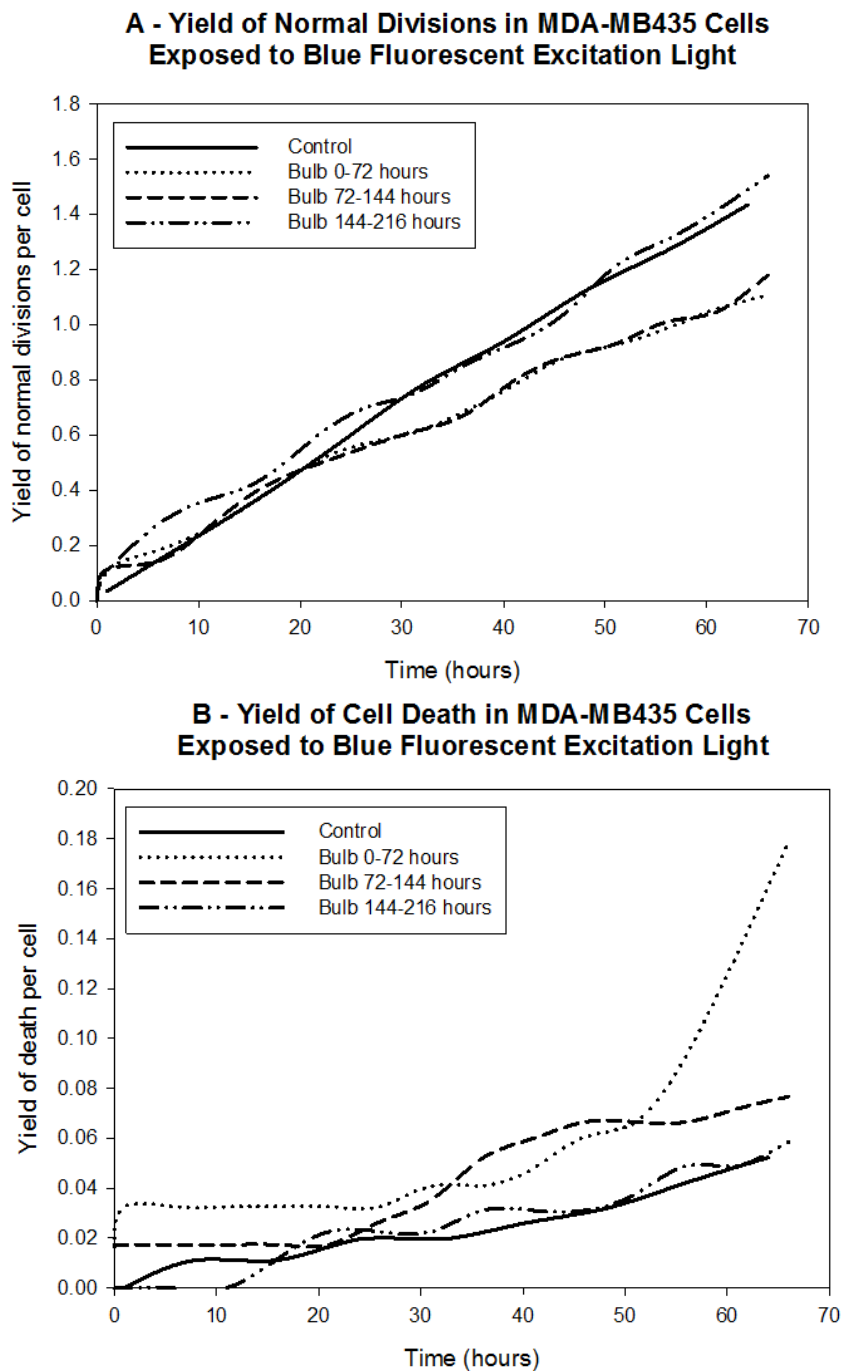
Figure 4.3: Yield of [A] normal divisions and [B] cell death in MDA-MB435 cells exposed to blue fluorescence excitation light. Four consecutive experiments were conducted, a control that acquired only grey scale images and three that acquired both fluorescent and grey scale images over the course of a mercury bulb's usable lifespan. Each experiment lasted for 3 days and in the treated samples, the cells received blue light for 1.5 seconds every 7 minutes.
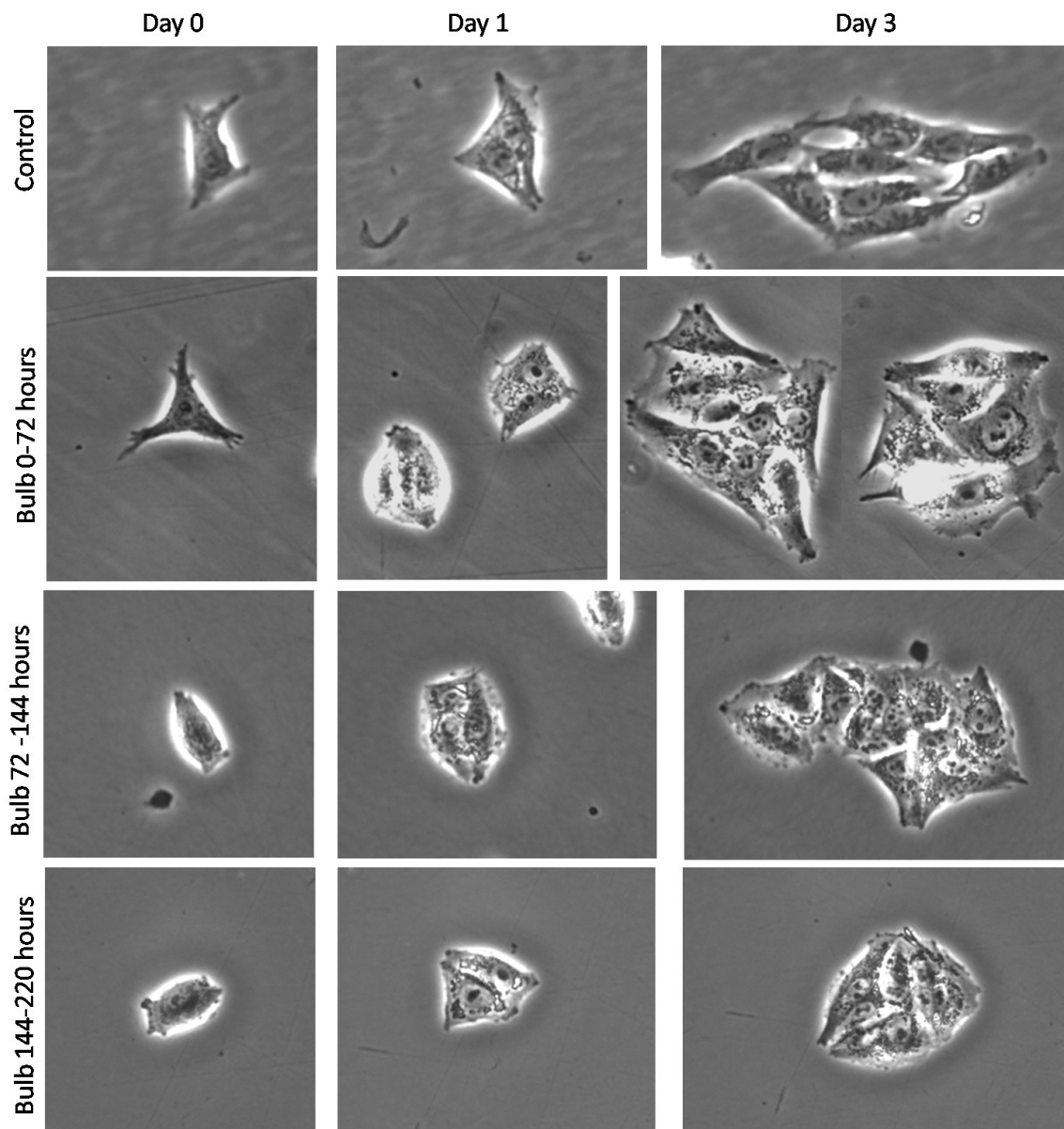
Figure 4.4: Morphology of MDA-MB435 cells exposed to blue fluorescence excitation light. These images were collected from digital image sequences of control cells and cells exposed to blue florescent light at days 0, 1 and 3 of image acquisition.
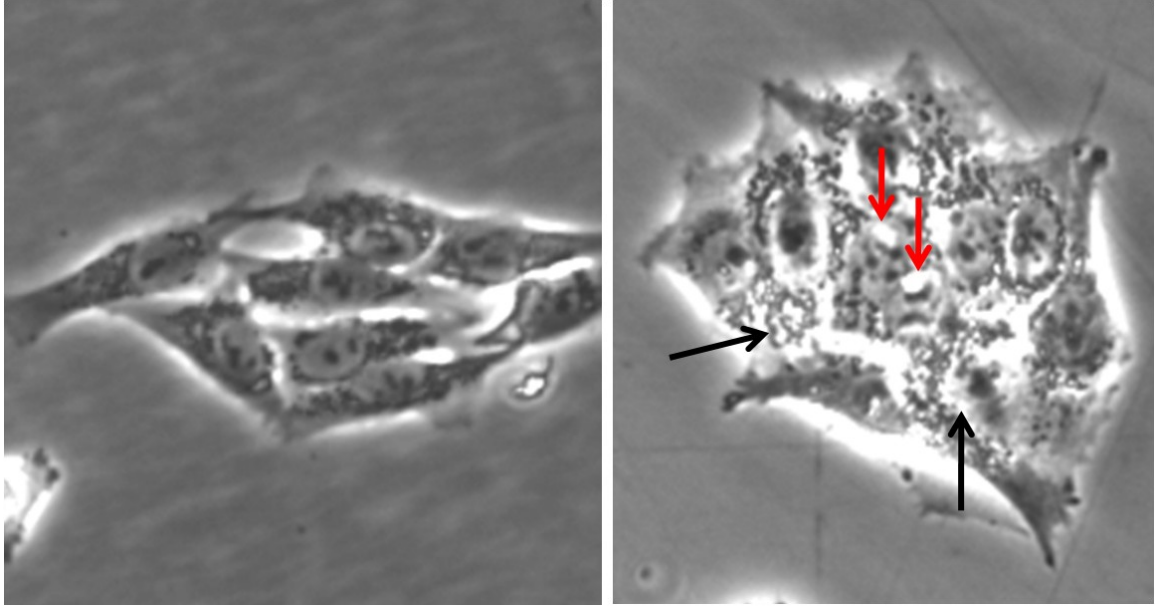
Figure 4.5: Morphology of MDA-MB435 cells exposed to blue fluorescence excitation light. at day 3 of image acquisition. [Left] Control cells show normal morphology after 3 days, no fluorescence excitation light was used. [Right] Cells exposed to blue fluorescence excitation light for 1.5s every 7 min for 3 days. Note the large cell size and formation of bright pixel areas in the exposed cell population.

CHAPTER 5

DISCUSSION AND CONCLUSIONS

Event Analysis for Live Cell Imaging

Presented here are new tools for the analysis of cellular data in digital image sequences. Live cell imaging is currently a fast growing field in cell research offering high throughput data for cellular response to damage or treatment as well as in elucidating cellular pathways via fluorescence detection of protein interactions. Digital image sequences of living cells contain data concerning the morphology of cells, cell clonogenicity, cell death, cell-cell interaction, and cell motility. Due to advancements in equipment for non-perturbing live cell imaging, correct design and implementation of an imaging system allows cells to be imaged on their normal substrate and medium furnishing data that are comparable to those obtained in parallel biochemical and molecular studies run in a laboratory. Combination of these techniques provides a novel method for connecting responses at the cellular level to those at the sub-cellular level which often require sacrifice of the cells. In order for these data comparisons to be made analytical methods are necessary for detecting observable cellular data within digital images and to measure the yield of events or search the data for patterns of events. These types of analyses are currently not available from commercial software packages; however the algorithms and programs described here were developed to serve these specific purposes. The information obtained by these analysis programs would normally take weeks or more to produce by hand.

The event analysis programs (Chapter 2) are designed to be extendable and easily modified to include new event types for application to a wide variety of experimental research. In the studies reported here we consistently applied cellular events related to cell division, cell fusion, and cell death. Using concepts from graph theory we chose to represent cell event data as tree structures enabling the use of subgraph isomorphisms to

detect patterns of events in the data. In addition this analysis methodology can be performed to calculate the overall yield of events regardless of event connectivity. After verifying internal algorithm consistency we applied these programs to two projects in the field of cancer research to demonstrate the program's effectiveness at measuring cell division and cell death parameters in living cells, as well as to show the powerful use of subgraph isomorphisms to detect rare event patterns in our data sets. We believe the observations and measurements presented here illustrate the novelty of the event analysis program, both as a substitute for traditional assays which measure cell clonogenicity or cell death, and as an addition to laboratory measurements typically used to elucidate molecular pathways involved in cancer.

## Event Analysis in Mitotic Catastrophe

Live cell imaging techniques were crucial to the analysis of events occurring during MC to gain information regarding the fate of cells undergoing MC. MC produces large multinucleated cells through rounds of failed and aborted mitoses. Through the use of the event analysis method we can now characterize the frequency of MC related abnormal divisions, cell fusions, and cell death. Importantly, we are now able to characterize the timing of the events occurring during and after MC. For example, we found that cell death after MC occurs at different times after many rounds of division post-irradiation, and that during these divisions MC cells give rise to mixed progeny colonies containing both large multinucleated and small mononucleated cells. The questions we were able to answer using our cell event data were: Do small mononucleated cells originate from an abnormal division event in a cell that has undergone radiation-induced MC? And, are those mononucleated progeny capable of resuming a normal growth pattern?

The analysis program was applied to two different cell lines treated with gamma radiation. The results reported in Chapter 3 showed that the production of MC cells is

more frequent than expected and that multipolar division events are enhanced in MC cells. Moreover, closer examination of the progeny resulting from the multipolar division types revealed that sometimes a mononucleated cell is produced from a multinucleated parent cell. Using the subgraph isomorphism algorithm, queries were designed to extract graphs containing this connectivity of events (MD|FMD → FO) and the data demonstrated that 7-9% of mononucleated cell progeny originate from multipolar divisions in MC cells produce in the two weeks subsequent to radiation treatment. It is important to remember that a potentially lethal tumor contains $\sim 10^{12}$ cells, and typically a cancer treatment must depress the curve of cell survival 9 logs to be considered effective (Ruddon, 2007). Thus, leaving $10^3$ cells to potentially proliferate and repopulate the tumor if they maintain their clonogenicity, and given some time, it takes only one clonogenic cell to produce a new tumor. We have shown that approximately 0.1% of irradiated cells can eventually give rise to a normally cycling cell and therefore this rare event is a true concern for cancer therapy. To this end the mechanism by which reductive, multipolar division occurs should be studied and possibly exploited to improve cancer treatments.

<div align="center">Mechanisms of Depolyploidization After Radiation</div>

<div align="center">Induced Mitotic Catastrophe</div>

For more than a decade our lab has studied the phenomenon of MC, reporting the formation of large, multinucleated cells following irradiation and other treatments. Previous experiments have focused on the morphological and molecular hallmarks of cells undergoing MC including over-production of cyclin B1, nuclear fragmentation, premature entry into mitosis, and notably the enhancement of MC in p53 mutant cell lines. As most solid tumors have non-functional p53 it was of interest to measure the frequency with which MC is induced and also to determine the fate of those cells. Using live cell imaging we were able to determine that MC cells are not limited to a fate of cell

death.  In fact, they are capable of reducing the number of sub-nuclei in their progeny through multipolar type divisions allowing them to regain a potentially more stable genome that might enable the MC progeny to remain viable.  In the experiments reported here we set out to determine the molecular pathways activated by cells that have undergone MC to promote multipolar division types and a possible route to survival.

The results reported in Chapter 3 show that these cells are able to reduce their DNA content over the time course that multipolar divisions were observed in digital image sequences.  These measurements led us to examine a naturally occurring form of reductive division, meiosis.  As the proteins and pathways activated during meiosis are well studied we were able to identify many genes that are specific to meiosis, and are up-regulated in our irradiated samples.  Using RT-PCR we were able to measure the up-regulation of meiosis-specific proteins such as DMC1, SYCP1-3, MOS, SPO11, Rad51AP2, Rec8, and STAG3; this technique measures gene expression at the transcriptional level through the detection of mRNA. To verify the translation of mRNA into functional proteins and correct localization within the cell, we utilized IF techniques. We found that many of these genes are indeed translated to protein, and interestingly the punctated patterns of SYCP3 staining are exactly as those found in pre-meiotic germ cells just before the initiation of meiosis and entry into prophase I (Prieto *et al*., 2004).  In rare cells we found extended or fiber-like SYCP3 staining similar to that present in gametic cells used as our positive controls in the IF experiments.

The implications for meiotic division in radiation induced MC cells extend beyond the ability of these cells to reduce their DNA content.  Meiosis is the source of variation within a species, meaning it is the method by which organisms recombine their DNA to produce offspring with genetic makeup that is not identical to their parents, thus ensuring diversity.  The process of meiotic recombination not only produces varied individuals but also provides a selective advantage if the recombination event produces a phenotype that promotes survival (reviewed by Barton and Charlesworth, 1998).

Therefore, it is possible to hypothesize that meiotic division and recombination events occurring in irradiated MC cells might confer a select advantage to these cells allowing them to overcome MC-related death. Further, resumption of a normal mitotic regimen in the survivors may produce a tumor well-adjusted to overall survival and potentially more resistant to treatment. Hence, determining the molecular mechanisms by which MC cells escape death and the potential for survival of their progeny is instrumental to creating new and enhanced tumor treatments.

## Event Analysis of Blue Fluorescence Excitation Light

### Toxicity

In the field of live cell imaging, probably the most modern and most widely used technique is the use of fluorescence detection for intracellular organelles, proteins, and molecules. While the technologies required to label and detect fluorescent molecules in a cell are well developed, they are not idealized for long term measurements as both the probes and excitation light are toxic to the cells [Wang and Nixon, 1978; Bradley and Sharkey, 1977; Hockberger *et al*., 1999; Goldman and Spector, 2005]. As always, we are committed to providing non-perturbing live cell measurements, to ensure accurate data and comparability to laboratory experiments. To this end, the event analysis program was applied to quantitatively describe the effect of blue fluorescence excitation light for cell division and cell death. For each experiment described (Chapter 4) we utilized cells that did not contain fluorescence proteins, probes, or dyes, thus ensuring all observations were elicited solely by the exposure to fluorescence excitation light.

It was determined that fluorescence light is toxic to multiple cell lines observed as the reduction of normal cell division, induction of cell death, and apparent morphological aberrations. While toxicity is carried across cell lines the degree of toxicity and possibly the mechanism, are not the same. In FaDu cells fluorescence excitation light greatly reduced the instance of normal divisions, however cell death was not observed to a large

degree unless the light intensity was under filtered. In MDA-MB435 cells, light toxicity induced cell death (with maximal filtering of light intensity) and reduced cell division though to a lesser degree than was observed in FaDu cells. Morphologically, both cell lines were less flattened to the cell surface during fluorescence excitation light exposure as compared to control cells. This effect was much more dramatic in the FaDu cells thus further morphological observations were hindered. However, the decreased attachment to the cell surface is an interesting observation because similar changes in geometry and pixel intensity at a cells' border can be seen when cells possibly modify membrane fluidity to undergo division. This suggests a mechanism may exist that induces damage at the level of the cell membrane during blue fluorescence excitation light exposure.

The MDA-MB435 cells are large (as compared to FaDu) and this facilitated additional observations during image analysis. It is apparent that areas of bright pixel intensity form in the MDA-MB435 cells starting approximately 24 hours after light exposure begins, and continuing to spread through the cell over the following 2 days. The observed areas of increase pixel intensity may be lipid vacuoles reported by Hockenburg *et al*. (1999) and can be confirmed in the future via electron microscopy. The formation of lipid vacuoles could be an effect of increased production of pro-oxidant molecules such as $H_2O_2$ which is metabolized by the cell to produce hydroxyl radicals which can interact with and damage the cell's macromolecules [Kellogg and Fridovich 1975, reviewed in Valko *et al*. 2004]. If indeed these effects are due to an increase in intracellular $H_2O_2$ the process should be dampened by the addition of catalase to promote the metabolic breakdown of $H_2O_2$ to $2H_2O$ and $O_2$. Additional experiments, such as the one suggested above should be conducted to further investigate the mechanism of fluorescence excitation light-induced cell toxicity. Further, the use of analytical equipment to measure the wavelengths of light output from the mercury bulb excitation source may provide insight concerning the most damaging wavelengths present in our system and the changes in wavelengths output over the usable lifetime of the bulb.

APPENDIX

MATERIALS AND METHODS

Cell Culture

HeLaS3, human cervical cancer cells, were grown in Joklik's Minimum Essential Medium (GIBCO); HeLa Clone3, human cervical cancer cells, were grown in Ham's F-10 Nutrient Mixture Medium (GIBCO); HCT116, human colon cancer cells, were grown in McCoy's 5A Modified Medium (GIBCO); MDA-MB435, human melanoma cells, were grown in high glucose Dulbecco's Modified Eagle's Medium (GIBCO). FaDu, human head and neck tumor cells were grown in Dulbecco's Modified Eagle's Medium (GIBCO)All media was supplemented with 10% fetal bovine serum (Hyclone) and antibiotics (100 U/ml penicillin and 100 μg/ml streptomycin; GIBCO). All cell lines were maintained in air incubators at 37°C and 5% $CO_2$.

Gamma Irradiation

Gamma-irradiation was delivered at the University of Iowa's Radiation Facility; cultures were irradiated at room temperature using a $^{137}Cs$ source (8,148 Ci) at the dose rate of 0.92 Gy/min. Sham irradiated control cells were transported with cells receiving treatment, and spent an equivalent amount of time exposed to room temperature.

Live Cell Imaging

Imaging was done at the LSDCAS core facility located at the Holden Comprehensive Cancer Center, University of Iowa, Iowa City, IA. LSDCAS consists of two live cell imaging systems capable of both phase-contrast and epi-fluorescence imaging (Figure 2.1). System 1 is comprised of an Olympus IX-70 inverted microscope, a Basler A630F CCD camera, and a custom built heat-controlled Plexiglas stage incubator. System 2 includes an Olympus IX-71 inverted phase microscope, a Hamamatsu ORCA-285 cooled CCD camera, and an Okolab stage incubator capable of

regulating $CO_2$, humidity, and temperature. In both systems the stage movement, illumination, auto-focusing, and image acquisition are under computer control. The software associated with operating the LSDCAS systems is developed and maintained in-house. Data acquisition is accomplished through the use of Linux software; archiving and analysis is performed using a collection of analysis software programs that run in Unix or Linux [Davis *et al.* 2007]. Images acquired by the microscope are temporarily stored a small server in the acquisition facility. After completion of the experiment, the images are automatically transferred to a data center where they can be accessed for analysis. The LSDCAS data center consists of a dual quad core server (16 gigabytes RAM – 5 terabytes RAID storage) and a HP Storageworks MSL2024 Ultrium 3, 10 terabyte tape library system for data back-up and archiving.

Cells were seeded up to twenty four hours prior to the start of imaging at a low density, between $5x10^4$ and $1x10^5$ cells/T-25 flask, or $2x10^4$ cells/well in a 6-well plate. Cells were allowed to attach to the flask surface in a dark incubator. Prior to transport, the plating media was replaced with $CO_2$ equilibrated media (unless stated otherwise) and the flask was closed. The flask was transported in a dark, warm box to prevent stress from light or low temperature exposure. Once the flask was secured on the microscope stage fields of view were selected using a joystick controller. When necessary the light exposure and gain were adjusted to accommodate varying cell types and their optical properties. At this time the fluorescence options were adjusted (for blue excitation light toxicity experiments); including interleave of gray scale:fluorescent image acquisition, the filter types or intensity, and the fluorescence excitation light exposure and gain. The images were collected on a small server in the acquisition facility and transferred for permanent storage once acquisition was complete.

## Manual Event Analysis

All cells in a field were initially identified (*IC, ICBN, ICMN*) and categorized as mononucleated, bi-nucleated or multinucleated. The images were then streamed forward until a visible event occured. Images were manually incremented or decremented to verify that the exact frame was in view. The center of the cell was right-clicked and the event selected from a drop down list. The "parent" event was highlighted when a new event was identified to maintain correct connectivity of events. The *casViewer* displays the parent event, this was verified by the user and when required, was corrected with the "drag-and-drop" function or by deleting and re-identifying the event. When a division event occurred the its type (*ND, FND, MD, FMD*) was categorized based on the number of mitotic poles the cell appeared to attempt and the number of daughter cells produced. The cells produced by a division event were identified immediately following division at the time they flattened out along the flask surface. The number of nuclei or sub-nuclei was indicated with the *flatten out* events (*FO, FOBN, FOMN*). Sister cell fusions have two parent events and both were verified when this event was identified. Non-sister cell fusions were identified twice if both cells were being analyzed, and once otherwise. Identification continued until the cell died (*DD, ID, DT, AP*), left the field of view (*OS*), or confluency/the end of the image sequence was reached (*EOA/EOM*).

## Cytological Preparations and DNA image cytometry

Harvested cells were pelleted then resuspended in 100% fetal calf serum. Approximately $8 \times 10^4$ cells were cytospun onto poly-L-lysine coated microscope slides and left to dry overnight. Samples were fixed in Acetone:100% EtOH (v:v), at 4°C for 30 minutes. Slides were allowed to dry for 15 min at r.t., followed by sample hydrolysis in 5N HCl at r. t. Hydrolysis proceeded 1 minute for morphology or 10 minutes for DNA measurements followed by 5 rinses in distilled $H_2O$ for 1 min each. Samples were stained using 0.05% Toloudine Blue in McIlvan's solution (pH 5 for morphology and

pH4 for DNA measurements) for 10 min at r.t. followed by a series of rinses in distilled H$_2$O until excess stain was removed. Next, samples were dehydrated by incubating slides twice in butanol at 37°C for 3 min. Sample clearing was then performed by incubating slides twice in xylene for 3 min. Finally, cover slips were mounted with Cytoseal 60 Mounting Media and morphology was evaluated under an Olympus B51 epifluorescence microscope.

DNA content was performed using ImagePro Plus 4.1 software. Slides were observed using a 100X oil immersion objective. The camera was set to examine change in green channel intensity; RGB channels were adjusted to keep the image background within 240-250 pixel intensity. The background intensity was verified at 6 random points spread across each image before analysis proceeded, to control for staining quality. Calibration was performed at each start of the program, using cells in telophase as a standard, until the error was calculated to be less than 10%. The slide was then examined for good candidates for measurement, meaning the stain is evenly distributed across the sample and sub-nuclei being measured do not overlap. When a good candidate was located the image was acquired, automatic borders were verified visually, and then manually adjusted when necessary. Parameters collected included: Area, diameter, margination, optical density, integrated optical density, clumpiness, and roundness.

<u>Immuno-fluorescence</u>

Harvested cells were pelleted and resuspended in 100% fetal calf serum, then a volume containing 8x10$^4$ cells was cytospun onto poly-L-lysine coated microscope slides. Fixation was determined from the antibody manufacturer either in ice-cold methanol (10-20 min), acetone (1-10 min) or 4% paraformaldehyde in PBS, pH7.4 (15 min). Slides were then washed twice in PBS at room temperature, and permeabilized for 10 min in PBS containing 0.25% Triton X-100. Slides were washed for 5 minutes in PBS three times, then blocked for 30 min in 1% BSA in PBS containing 0.05% Tween-20

(PBST). The appropriate dilution of antibody was applied to each sample and slides were incubated overnight at 4°C. The next day, slides were washed three times in PBST for 5 minutes each time. Secondary antibodies were applied at the appropriate dilutions and slides incubated at r.t. in the dark for 1 hour, then washed three times in PBST for 5 minutes each time. Antibodies were diluted in 1% BSA in PBST. Samples were counterstained and mounted with DAPI Vectashield Mounting Media (Vector Laboratories) and evaluated under an Olympus B51 epifluorescence microscope.

*Primary antibodies*:

Anti-CyclinB1 (Millipore cat. 05-373) 1:25

Anti-DMC1 (Abcam cat. Ab-11054) 1:100

Anti-SYCP3 (Abcam cat. Ab-15093) 1:50

*Secondary antibodies*:

AlexFluor 488 F(ab')2 fragment of goat anti-mouse IgG (H+L) (Invitrogen cat. A11017) 1:500

AlexFluor 568 F(ab')2 fragment of goat anti-rabbit IgG (H+L) (Invitrogen cat. A21069) 1:500

FITC conjugated goat anti-mouse IgG (Sigma cat. F5897) 1:1000

## Quantitative Real-Time Reverse Transcriptase Polymerase
## Chain Reaction (qRT-PCR) Assay

Total RNA was extracted using the RNeasy Mini Kit (Qiagen) according to the manufacturer's protocol. cDNA was synthesized using SuperScript II RT (Invitrogen) according to the manufacturer's protocol. Reverse transcription was performed using 1μg of total RNA and a mixture of oligo(dT) and random hexamer primers as described in Bieche and collaborators (2000). One-twentieth of this reaction, or cDNA corresponding to 50 ng RNA, was used for PCR. PCR was performed using Immolase DNA Polymerase (Bioline) in 20 μl reactions containing, 1X Immolase buffer, 1.5 mM

MgCl, 200 µM each dNTP, 200 nM each primer, 200 nM probe, and 0.75 U Immolase. Primers and FAM-labeled probes were obtained from Applied Biosystems Inc.. Reactions were performed in triplicate with the DNA Engine  Opticon 2 Thermalcycler (MJ Research-Bio-Rad) using the following cycling parameters:  94ºC for 10 minutes followed by 40 cycles of 95ºC for 15 seconds and 60ºC for 1 minute. The 60S acidic ribosomal protein P0 was used as a control to normalize for pipetting error.   Data was analyzed using Opticon Monitor Analysis Software Version 2.02 (MJ Research) and quantified using a standard curve constructed of known copy number of p-GEM-T PCR cloning vector (Promega) containing PCR amplicon in the multiple cloning region.

## Superarray RT-PCR Assay

Total RNA extraction was performed as reported above using an RNeasy Mini Kit (QIAGEN). The $RT^2$ First Strand Kit (SuperArray cat #C-03) was used to eliminate genomic DNA and reverse transcribe 1µg of total RNA to cDNA.  The template DNA was next added to the $RT^2$ SYBR Green qPCR Master Mix (SuperArray cat. #PA-010) and 25 µl loaded into each well of the $RT^2$ Profiler PCR Array (SuperArray cat. #CAPH-0492). The Superarray was custom designed to contain primers for the following genes: SYCP1, SYCP2, SYCP3, RAD51AP2. SPO11, REC8, DMC1, MOS, STAG3, and CCNB1 (cyclin B1).  The PCR reactions were run in a DNA Engine Opticon 2 Thermalcycler (MJ Research-Bio-Rad) using the following cycling parameters: 40 cycles of 95°C for 15 seconds, 55°C for 30 seconds, and 70°C for 30 seconds, cycles were followed by a melting curve analysis to verify product purity. The data was analyzed using the $2^{-\Delta\Delta Ct}$ method with two separate housekeeping genes, ACTB (b-actin) and RPLP0, and reported as fold increase over control.

# REFERENCES

Adamah D.J.B., Gokhale P.J., Eastwood D.J., Goepel J., Walsh J.R., Moore H.D., Andrews P.W.. 2006. Dysfunction of the mitotic:meiotic switch as a potential cause of neoplastic conversion of primordial germ cells. *Intl Journ of Andrology*. 29: 219-227.

Barber T.D., McManus K., Yuen K.W.Y., Reis M., Parmigiani G., Shen D., Barrett I., Nouhi Y., Spencer F., Markowitz S., Velculescu V., Kinzler K., Vogelstein B., Lengauer C., Hieter P.. 2008. Chromatid cohesion defects may underlie chromosome instability in human colorectal cancers. *Proc Natl Acad Sci*. 105(9): 3443-3448.

Barton N.H. and Charlesworth B.. 1998. Why sex and recombination? *Science*. 281:1986-1990.

Berztiss A.T.. 1973. A backtrack procedure for isomorphism of directed graphs. *Journal of the Assoc. for Computing Machinery*. 20(3): 365-377.

Bradley M.O., Sharkey N.A.. 1977. Mutagenicity and toxicity of visible fluorescent light to cultured mammalian cells. *Nature*. 266: 724-6.

Castedo M., Perfettini J.L., Roumier T., Andreau K., Madema R., Kroemer G.. 2004. Cell death by mitotic catastrophe: a molecular definition. *Oncogene*. 23: 2825-2837.

Cohen P.E., Pollack S.E., Pollard J.W.. 2006. Genetic analysis of chromosome pairing, recombination, and cell cycle control during the first meiotic prophase. *Endocrine Reviews*. 27(4):398-426.

Conrad C., Erfle H., Warnat P., Daigle N., Lörch T., Ellenberg J., Pepperkok R., Eils R.. 2004. Automatic identification of subcellular phenotypes on human cell arrays. *Genome Res*. 14:1130-1136.

Crawford L.V., Pim D., Lamb P.. 1984. The cellular protein p53 in human tumours. *Molec. biol. Med*. 2:261−272.

Davis P.J., Kosmacek E.A., Yuansheng S., Ianzini F., Mackey M.A.. 2007. The Large-Scale Digital Cell Analysis System: an open system for non-perturbing live cell imaging. *Journal of Microscopy*. 228: 296-308.

Erenpreisa J. and Cragg M.S.. 2001. Mitotic death: a mechanism of survival? A review. *Cancer Cell International*. 1:1.

Erenpreisa J. and Cragg M.S.. 2005. Mitotic catastrophe and endomitosis in tumor cells: An evolutionary key to a molecular solution. *Cell Biology International*. 29(12):1012-1018.

Erenpreisa J., Kalejs M., Ivanov A., Illidge T.M., Ianzini F., Kosmacek E.A., Mackey M.A., Dalmane A., Cragg M.S.. 2005. Genomes Segregation in Polyploid Tumor Cells Following Mitotic Catastrophe. *Cell Biology International*. 29:1005-1011.

Erenpreisa J., Ivanov A., Wheatley S.P., Kosmacek E.A., Ianzini F., Anisimov A.P., Mackey M.A., Davis P.J., Plakhins G., Illidge T.M.. 2008. Endopolyploidy in irradiated p53-deficient tumour cell lines: persistence of cell division activity in giant cells expressing Aurora-B kinase. *Cell Biology International*. 32(9):1044-1056.

Fukasawa K. and Vande Woude G.F.. 1995. Mos overexpression in Swiss 3T3 cells induces meiotic-like alterations of the mitotic spindle. *Proc Natl Acad Sci*. 92: 3430-3434.

Goldman RD and Spector DL. 2005. *Live cell imaging: A laboratory manual*. Cold Spring Harbor, NY: Cold Spring Harbor Laboratory Press.

Gorgoulis V.G., Zacharatos P., Mariatos G., Liloglou T., Kokotas S., Kastrinakis N., Kotsinas K., Athanasiou A., Foukas P., Zoumpourlis V., Kletsas D., Ikonomopoulos J., Asimacopoulos P.J., Kittas C., Field J.K.. 2001. Deregulated expression of *c-mos* in non-small cell lung carcinomas: relationship with p53 status, genomic instability, and tumor kinetics. *Cancer Research*. 61: 538-549.

Hall, Eric. 2006. *Radiobiology for the Radiobiologist*. Philadelphia, PA: Lippincott Publishers.

Harada H., Nagai H., Tsuneizumi M., Mikami I., Sugano S., Emi M.. 2001. Identification of DMC1, a novel gene in the TOC region on 17q25.1 that shows loss of expression in multiple human cancers. *Journal of Human Genetics*. 46: 90-95.

Hinchcliffe E.H.. 2005. Using long-term time-lapse imaging of mammalian cell cycle progression for laboratory instruction and analysis. *Cell Biology Education* 4:284-290.

Hockberger P.E., Skimina T.A., Centonze V.E., Lavin C., Chu S., Dadras S., Reddy J.K., White J.G.. 1999. Activation of flavin-containing oxidases underlies light-induced production of $H_2O_2$ in mammalian cells. *Proc Natl Acad Sci*. 96: 6255-6260.

Ianzini F. and Mackey M.A.. 1997. Spontaneous premature chromosome condensation and mitotic catastrophe following irradiation of HeLaS3 cells. *International Journal of Radiation Biology*. 72(4): 409-421.

Ianzini F. and Mackey M.A.. 1998. Delayed DNA damage associated with mitotic catastrophe following x-irradiation of HeLa S3 cells. *Mutagenesis* 13:337-344.

Ianzini F., Cherubini R., Mackey M.A.:1999. Mitotic catastrophe induced by exposure of V79 Chinese hamster cells to low energy protons. *Int J Radiat Biol.* 75: 717-723.

Ianzini F. and Mackey M.A.. 2002. Development of the large scale digital cell analysis system. *Radiation Protection* Dosimetry. 99: 289-293.

Ianzini F., Bertoldo A., Kosmacek E.A., Phillips S.L., Mackey M.A.. 2006. Lack of p53 function promotes radiation-induced mitotic catastrophe in mouse embryonic fibroblast cells. *Cancer Cell International*. 6(11): doi:10.1186/1475-2867-6-11.

Ianzini F. and Mackey M.A.. 2007. Mitotic Catastrophe. In *Apoptosis, Senescence and Cancer, Second Edition,* Edited by Gewirtz D.A., Holt S.E., Grant S., Humana Press:73-91.

Ianzini F, Kosmacek EA, Nelson ES, Napoli E, Erenpreisa J, Kalejs M, Mackey MA. Activation of Meiosis-Specific Genes is Associated with Depolyploidization of Human Tumor Cells Following Radiation-Induced Mitotic Catastrophe. 2009. *Cancer Res,* 69:2296-2304.

Kaljes M., Ivanov A., Plakhins G., Cragg M., Emzinsh D., Illidge T., Erenpresia J.. 2006. Upregulation of meiosis specific genes in lymphoma cell lines following genotoxic insult and induction of mitotic catastrophe. *BMC Cancer.* 6:6-16.

Karolchik D., Kuhn, R.M., Baertsch R., Barber G.P., Clawson H., Diekhans M., Giardine B., Harte R.A., Hinrichs A.S., Hsu F., Miller W., Pedersen J.S., Pohl A., Raney B.J., Rhead B., Rosenbloom K.R., Smith K.E., Stanke M., Thakkapallayil A., Trumbower H., Wang T., Zweig A.S., Haussler D., Kent W.J.. 2008. The UCSC Genome Browser Database: 2008 update. *Nucleic Acids Res.* 36:D773-9.

Kellogg E.W. and Fridovich I.. 1975. Superoxide, hydrogen peroxide, and singlet oxygen in lipid peroxidation by a xanthine oxidase system. *J Bio Chem.* 250(22): 8812-8817

Knight M.M., Roberts S.R., Lee D., Bader D.L.. 2003. Live cell imaging using confocal microscopy induces intracellular calcium transits and cell death. *Am J Physiol Cell Physiol.* 284(4):C1083-C1089.

Kosmacek E.A., Mackey M.A., Davis P. J., Ianzini F.. Identification and statistical analysis of cellular events detected in living cells using the Large Scale Digital Cell Analysis System. *BMC Bioinformatics.* 2009, *submitted.*

Krissnel E.B. and Henrick K.. 2004. Common subgraph isomorphism detection by backtracking search. *Softw. Pract. Exper.* 34: 591-607.

Levi G.. 1972. A note on the derivation of maximal common subgraphs of two directed or undirected graphs. *Calcolo* 9:341–354.

McGregor J.. 1982. Backtrack search algorithms and the maximal common subgraph problem. *Software—Practice and Experience* 12:23–34.

Mackey M.A., Morgan W.F., Dewey W.C.. 1988. Nuclear fragmentation and premature chromosome condensation induced by heat shock in S-phase Chinese hamster ovary cells. *Cancer Res.* 48: 6478-6483.

Mackey M.A. and Ianzini F.. 2000. Enhancement of Radiation-Induced Mitotic Catastrophe by Moderate Hyperthermia. *Int J Radiat Biol.* 76: 273-280.

Molz L., Booher R., Young P., Beach D.. 1989. *cdc2* and the regulation of mitosis: six interacting *mcs* genes. *Genetics.* 122: 773-782

Morimura Y., Kotin P., Falk H.L.. 1964. Photodynamic toxicity of polycyclic aromatic hydrocarbons in tissue culture. *Cancer Research.* 24: 1249-1259.

Pines J. and Hunter T.. 1991. Human cyclins A and B1 are differentially located in the cell and undergo cell cycle-dependant nuclear transport. *J Cell Biol.* 115:1-17.

Prieto I., Tease C., Pezzi N., Buesa J.M., Ortega S., Kremer L., Martinez A., Martinez-A C., Hulten M.A, Barbero J.L.. 2004. Cohesin component dynamics during meiotic prophaee I in mammalian oocytes. *Chromosome Res.* 12:197-213.

Propst F. and Vande Woude G.F.. 1985. Expression of c-mos proto-oncogene transcripts in mouse tissues. *Nature.* 315: 516-518.

Raderschall E., Stout K., Freier S., Suckow V., Schweiger S., Haaf T.. 2002. Elevated levels of rad51 recombination protein in tumor cells. *Cancer Research.* 62: 219-225.

Rae J.M., Creighton C.J., Meck J.M., Haddad B.R., Johnson M.D.. 2007. MDA-MB435 cells are derived from M14 melanoma cells – a loss for breast cancer, but a boon for melanoma research. *Breast Cancer Res Treat.* 104:13-19.

Revenkova E. and Jessberger R.. 2006. Shaping meiotic chromosomes: cohesins and synaptonemal complex proteins. *Chromosoma.* 115:235-240.

Rieder C.L. and Khodjakov A.. 2003. Mitosis through the microscope: Advances in seeing inside live dividing cells. *Science* 300:91-96.

Romanienko P. and Camerini-Otero R.D.. 1999. Cloning, Characterization, and Localization of Mouse and Human *SPO11. Genomics.* 61(2): 156-169.

Ross D.T., Scherf U., Eisen M.B., Perou C.M., Rees C., Spellman P., Iyer V., Jeffrey S.S., Van de Rijn M., Waltham M., Pergamenschikov A., Lee J.C., Lashkari D., Shalon D., Myers T.G., Weinstein J.N., Botstein D., Brown P.O.. 2000. Systematic variation in gene expression patterns in human cancer cell lines. *Nat. Genet.* 24**:**227-235.

Ruddon, R.W.. 2007. *Cancer Biology, Edition 4.* New York, NY:Oxford University Press.

Russel P. and Nurse P.. 1987. Negative regulation of mitosis by *wee1+*, a gene encoding a protein kinase homolog. *Cell.* 49: 559-567.

Steel G.G., Adams K., and Barratt J.C.. 1966. Analysis of the cell population kinetics of transplanted tumours of widely-differing growth rate. *Brit.* J. *Cancer.* 20(4): 784-800.

Stephens D.J. and Allan V.. 2003. Light microscopy techniques for live cell imaging. *Science* 300:82-86.

Taylor W.R. and Stark G.R.. 2001. Regulation of the G2/M transition by p53. *Oncogene.* 20:1803-1815.

Ullmann J.R.. 1976. An algorithm for subgraph isomorphism. *Journal of the Assoc. for Computing Machinery.* 23(1): 31-42.

Valko M., Izakovic M., Mazur M., Rhodes C.J., Telser J.. 2004. Role of oxygen radicals in DNA damage and cancer incidence. *Mol Cel Biochem.* 266: 37–56.

Vogelstein B. and Kinzler KW.. 1992. p53 function and dysfunction. *Cell.* 70:523-526.

Wang RJ and Nixon BR. Identification of hydrogen peroxide as a photoproduct toxic to human cells in tissue-culture medium irradiated with "daylight" fluorescent light. *In Vitro.* 1978, 14(8): 715-22.

West, DB. *Introduction to Graph Theory.* 1996. Prentiss Hall, Upper Saddle River, NJ.

Westendorf J.M., Swenson K.I., Ruderman J.V.. 1989. The role of cyclin B in meiosis. *J Cell Biol*. 108:1431-1444.